The Astrophysical Journal, 1009:241 (17pp), 2026 October 1 https://doi.org/10.3847/1538-4357/ae9bbf
© 2026. The Author(s). Published by the American Astronomical Society.
OPEN ACCESS

JWST Nebular Spectroscopy of SN 2023qov: Circumstellar Dust Emission in a Normal Type Ia Supernova

Colin W. Macrie[1,2], Conor Larison[3], Huei Sears[2], Lindsey A. Kwok[4,40], Saurabh W. Jha[2], Mi Dai[5], Joel Johansson[6], Stéphane Blondin[7,8], Moira Andrews[9,10], K. Auchettl[11,12], Carles Badenes[5], Barnabás Barna[13,14], K. Azalee Bostroem[15], Thomas G. Brink[16], Kyle W. Davis[12], Joseph R. Farah[9,10], Alexei V. Filippenko[16], Ori D. Fox[3], Or Graur[17,18], Saarah Hall[4,19], D. Andrew Howell[9,10], Griffin Hosseinzadeh[20], Anders Jerkstrand[6], Réka Könyves-Tóth[21,22], C. Lidman[23], Keiichi Maeda[24], Kate Maguire[25], Bailey Martin[23], Adam Miller[4,19,26], Megan Newsome[9,10,27], Estefania Padilla Gonzalez[28], Abigail Polin[1], Armin Rest[3,28], Zoe A. Rosenberg[29], David J. Sand[15], Michaela Schwab[30], Matthew R. Siebert[3], Mridweeka Singh[31], Tamás Szalai[13,32], Tea Temim[33], Jacco H. Terwel[25], Brad E. Tucker[34,35], József Vinkó[13,21,36], Lingzhi Wang[37,38], Xiaofeng Wang[39], and WeiKang Zheng[16]

[1] Department of Physics and Astronomy, Purdue University, 525 Northwestern Avenue, West Lafayette, IN 47907-2036, USA; cmacrie@purdue.edu
[2] Department of Physics and Astronomy, Rutgers, the State University of New Jersey, Piscataway, NJ 08854, USA
[3] Space Telescope Science Institute, 3700 San Martin Drive, Baltimore, MD 21218, USA
[4] Center for Interdisciplinary Exploration and Research in Astrophysics (CIERA), Northwestern University, Evanston, IL 60208, USA
[5] Department of Physics and Astronomy and PITT PACC, University of Pittsburgh, Pittsburgh, PA 15260, USA
[6] Department of Physics, Oskar Klein Centre, Stockholm University, SE-106 91, Stockholm, Sweden
[7] European Southern Observatory, Karl-Schwarzschild-Str. 2, 85748, Garching, Germany
[8] Aix-Marseille Université, CNRS, CNES, LAM, Marseille 13007, France
[9] Las Cumbres Observatory, 6740 Cortona Dr. Suite 102, Goleta, CA 93117, USA
[10] Department of Physics, University of California, Santa Barbara, Santa Barbara, CA 93106, USA
[11] School of Physics, The University of Melbourne, Parkville, VIC 3052, Australia
[12] Department of Astronomy and Astrophysics, University of California, Santa Cruz, CA 95064, USA
[13] Department of Experimental Physics, Institute of Physics, University of Szeged, Dóm tér 9, 6720 Szeged, Hungary
[14] HUN-REN-SZTE Stellar Astrophysics Research Group, 6500 Baja, Szegedi út, Kt. 766, Hungary
[15] Steward Observatory, University of Arizona, 933 North Cherry Avenue, Tucson, AZ 85721-0065, USA
[16] Department of Astronomy, University of California, Berkeley, CA 94720-3411, USA
[17] Institute of Cosmology and Gravitation, University of Portsmouth, Portsmouth, PO1 3FX, UK
[18] Department of Astrophysics, American Museum of Natural History, Central Park West and 79th Street, New York, NY 10024-5192, USA
[19] Department of Physics and Astronomy, Northwestern University, 2145 Sheridan Road, Evanston, IL 60208, USA
[20] Department of Astronomy & Astrophysics, University of California, San Diego, 9500 Gilman Drive, MC 0424, La Jolla, CA 92093-0424, USA
[21] HUN-REN Research Centre for Astronomy and Earth Sciences, Konkoly Observatory, Konkoly Th. M. út 15-17, 1121 Budapest, Hungary
[22] CSFK, MTA Centre of Excellence, Konkoly Thege Miklós út 15-17, 1121 Budapest, Hungary
[23] The Research School of Astronomy and Astrophysics & Centre for Gravitational Astrophysics, The Australian National University, Canberra, ACT 2611, Australia
[24] Department of Astronomy, Kyoto University, Kitashirakawa-Oiwake-cho, Sakyo-ku, Kyoto 606-8502, Japan
[25] School of Physics, Trinity College Dublin, College Green, Dublin 2, Ireland
[26] NSF-Simons AI Institute for the Sky (SkAI), 172 E. Chestnut St., Chicago, IL 60611, USA
[27] Department of Physics and Astronomy, University of Texas Austin, 2515 Speedway, Austin, TX 78712, USA
[28] Physics and Astronomy Department, Johns Hopkins University, Baltimore, MD 21218, USA
[29] Center for Computational Relativity and Gravitation, Rochester Institute of Technology, Rochester, NY 14623, USA
[30] Department of Astronomy, University of Virginia, 530 McCormick Road, Charlottesville, VA 22904, USA
[31] Indian Institute of Astrophysics, Koramangala 2nd Block, Bangalore 560034, India
[32] MTA-ELTE Lendület "Momentum" Milky Way Research Group, Szent Imre H. st. 112, 9700 Szombathely, Hungary
[33] Department of Astrophysical Sciences, Princeton University, Princeton, NJ 08544, USA
[34] Mt Stromlo Observatory, The Research School of Astronomy and Astrophysics, Australian National University, ACT 2611, Australia
[35] Australian National Centre for the Public Awareness of Science, Australian National University, ACT 2601, Australia
[36] ELTE Eötvös Loránd University, Institute of Physics and Astronomy, Pázmány Péter sétány 1, Budapest 1117, Hungary
[37] College of Science, Hainan Tropical Ocean University, Sanya 572022, People's Republic of China
[38] Chinese Academy of Sciences South America Center for Astronomy (CASSACA), National Astronomical Observatories, CAS, Beijing 100101, People's Republic of China
[39] Department of Physics, Tsinghua University, Beijing 100084, People's Republic of China
Received 2026 April 9; revised 2026 August 8; accepted 2026 August 14; published 2026 September 30

Abstract

We present panchromatic observations of the Type Ia supernova (SN Ia) 2023qov, ranging from ∼2 weeks before to ∼1 yr after maximum light. JWST near- and mid-infrared spectra at +276 and +363 days show ∼400 K dust emission that cools by ∼75 K between epochs, the first unambiguous spectroscopic detection of dust emission in a

[40] NASA Hubble Fellow.

Original content from this work may be used under the terms of the Creative Commons Attribution 4.0 licence. Any further distribution of this work must maintain attribution to the author(s) and the title of the work, journal citation and DOI.

normal SN Ia. We find that the emission is well described by models of carbonaceous dust placed within ∼1 lt-yr of the SN, with a dust mass of $\sim 10^{-4}\,M_{\odot}$. We do not see evidence of active dust creation, suggesting an infrared light echo by preexisting circumstellar dust as the likely source of the emission. The JWST nebular line profiles suggest asymmetric, stratified ejecta, similar to other normal SNe Ia, though a slight double-horn structure in the argon lines indicates a toroidal enhancement. SN 2023qov exhibits a slightly red, fast-declining early light curve ($\Delta m_{15}(B) = 1.47 \pm 0.05$ mag), from which we determine a ^{56}Ni mass of $M_{56} = 0.21 \pm 0.04\,M_{\odot}$, and a distance of $d = 36.0 \pm 1.8$ Mpc to the SN and its host, NGC 7029. The presence of circumstellar dust around a normal SN Ia has implications both for the progenitor system, suggesting a less than pristine environment, and for cosmology, as a possible source of reddening and extinction that can affect distance inferences.

Unified Astronomy Thesaurus concepts: Supernovae (1668); Type Ia supernovae (1728); James Webb Space Telescope (2291)

Materials only available in the online version of record: data behind figures

1. Introduction

Type Ia supernovae (SNe Ia) are the thermonuclear explosions of carbon–oxygen white dwarfs in binary systems (F. Hoyle & W. A. Fowler 1960). Though they are used extensively as distance indicators in cosmological studies (e.g., M. M. Phillips 1993; R. Tripp 1998), including in the discovery of the accelerating expansion of the Universe (A. G. Riess et al. 1998; S. Perlmutter et al. 1999), their progenitor systems and explosion mechanisms are not concretely understood. In current literature, there are two primary progenitor models: a single-degenerate (SD) scenario where a white dwarf interacts with a main-sequence, red-giant, or helium-star companion, or a double-degenerate (DD) system comprised of a pair of white dwarfs. Further, multiple explosion mechanisms are possible, with models that span a range of deflagration and detonation scenarios (for recent reviews, see Z.-W. Liu et al. 2023; A. J. Ruiter & I. R. Seitenzahl 2025; S. Blondin 2026).

Contemporary observations have brought a wealth of SN Ia data to address these questions (S. W. Jha et al. 2019). High-cadence surveys, including both widefield (T. W.-S. Holoien et al. 2017; J. L. Tonry et al. 2018; E. C. Bellm et al. 2019) and targeted programs (L. Tartaglia et al. 2018; K. Itagaki 2020), enable the early discovery of nearby SNe. Comprehensive datasets of these objects now often include ultraviolet (UV) through near-infrared (NIR) photometry and spectroscopy (e.g., J. M. Silverman et al. 2012; P. J. Brown et al. 2014; N. Morrell et al. 2024; S. Tinyanont et al. 2024). A new addition is late-time nebular NIR and mid-infrared (MIR) spectroscopy with JWST (e.g., J. M. DerKacy et al. 2023, 2024; L. A. Kwok et al. 2023, 2024, 2025, 2026; C. Ashall et al. 2024; M. R. Siebert et al. 2024). Extensive studies of individual, nearby SNe Ia provide our best avenue for understanding their astrophysical origins.

Spectral time series offer an in-depth, evolving view of an SN by revealing continuously deeper layers of the SN ejecta as the photosphere recedes into the innermost, lower-velocity regions. At late times ($\gtrsim$150 days postmaximum; see C. Fransson & A. Jerkstrand 2015), the SN Ia ejecta become increasingly optically thin, allowing us to see through the SN and directly observe the velocity structure of the elements synthesized in the explosion (e.g., A. Jerkstrand et al. 2015). Importantly, with late-time JWST observations, we can observe nebular lines of intermediate-mass elements (IMEs; e.g., Si, Ar, and Ca) and iron-group elements (IGEs; e.g., Fe, Co, and Ni) whose abundances are sensitive to the density and temperature structure of the progenitor. JWST observations of several normal SNe Ia (e.g., SN 2021aefx, J. M. DerKacy et al. 2023; L. A. Kwok et al. 2023; C. Ashall et al. 2024; SN 2022aaiq and SN 2024gy, L. A. Kwok et al. 2026) have shown strong central emission from stable nickel, indicative of high-density burning (S. Blondin et al. 2022)—perhaps implying a near-Chandrasekhar-mass white dwarf progenitor—as well as IME line profiles that provide evidence for stratified ejecta, a hallmark of detonations (e.g., delayed detonation or double detonation).

With a growing sample of JWST observations of SNe Ia, we can begin to connect these nebular, NIR+MIR SN properties to their host-galaxy environments. SN 2022aaiq (L. A. Kwok et al. 2026) and SN 2023qov occurred in quiescent host galaxies, while SN 2021aefx (J. M. DerKacy et al. 2023; L. A. Kwok et al. 2023; C. Ashall et al. 2024), SN 2022xkq (J. M. DerKacy et al. 2024), and SN 2024gy (L. A. Kwok et al. 2026) are in star-forming hosts. Evidence shows that SN Ia peak luminosity and light-curve evolution are environment dependent (D. Branch et al. 1996; M. Hamuy et al. 1996, 2000; M. Sullivan et al. 2006, 2010; M. Rigault et al. 2013; X. Wang et al. 2013, 2019). Samples of normal SNe Ia exhibit a bimodal distribution of the decline rate (R. Wojtak et al. 2023; C. Larison et al. 2024; R. Senzel et al. 2025; E. Padilla Gonzalez et al. 2026), with the hosts of the faster-declining SNe occurring being older galaxies with low star formation rates (M. Rigault et al. 2020). The slower-evolving SNe Ia usually occur in star-forming galaxies. Conversely, the peak colors of SNe Ia appear unimodal, not depending on the host environment (R. Wojtak et al. 2023; C. Larison et al. 2024; R. Senzel et al. 2025). Different progenitors could explain the bimodality in the decline rate, as older stellar populations may support different progenitor systems. If progenitor-system characteristics were to explain this bimodality, differences between the two populations could be revealed in nebular NIR+MIR emission.

SNe Ia are the main contributors to the chemical enrichment of the Universe with IGEs (K. Nomoto et al. 2013). However, when it comes to dust, there has been little observational evidence to suggest that normal SNe Ia contribute to the formation of interstellar dust (C. L. Gerardy et al. 2007; H. L. Gomez et al. 2007). Thermonuclear SNe are expected to be hostile to preexisting dust, destroying any created by the progenitor system during the explosion (H. L. Morgan & M. G. Edmunds 2003).

Some work has already been done to constrain the possibility of circumstellar material (CSM) around normal SNe Ia with large samples in the NIR (K. Maeda et al. 2015), MIR (J. Johansson et al. 2013), and radio (L. Chomiuk et al.

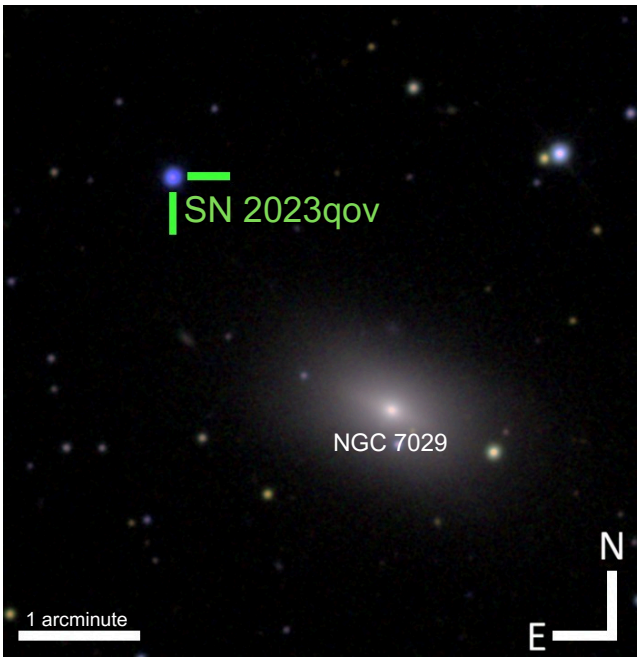


Figure 1. Las Cumbres Observatory *gri* image of SN 2023qov and its elliptical host galaxy NGC 7029 four days before peak brightness. Based on our computed distance to SN 2023qov and the angular separation, its projected distance is 28 kpc from the host center.

2016). These have revealed that many observations of normal SNe Ia have not yet ruled out CSM presence altogether, and have given upper limits of preexplosion mass loss ranging from 10^{-9} to $10^{-4}\,M_{\odot}\,\mathrm{yr}^{-1}$. Further, recent evidence has shown that peculiar SN Ia environments are not as clean as previously thought. Late-time MIR emission from the peculiar SN Ia, SN 2018evt (L. Wang et al. 2024), revealed $\sim 10^{-2}\,M_{\odot}$ of dust formation at $\gtrsim$1000 days postexplosion. This dust creation is thought to be powered by the interaction between the SN ejecta and hydrogen-rich CSM, similar to the Type Ia-CSM SN 2005gj (O. D. Fox & A. V. Filippenko 2013).

Recently, evidence for dust has also arisen in peculiar SNe Ia not normally associated with rich CSM, with G. Mo et al. (2025) reporting MIR rebrightenings in five SNe Ia of the peculiar "Iax" (SNe Iax) (R. J. Foley et al. 2013), "91T-like" (A. V. Filippenko et al. 1992b; M. M. Phillips 1993), and "03fg-like" (D. A. Howell et al. 2006) subtypes. A similar rebrightening was observed in the Type Iax SN 2014dt (O. D. Fox et al. 2016). This, combined with improved modeling (e.g., A. Kumar & A. Sarangi 2026), has shown that low-luminosity thermonuclear SNe, such as SNe Iax, are strong candidates to contribute to interstellar dust populations.

Despite these advances, the potential origin of dust in SNe Ia is not well understood. JWST MIR spectroscopy of the peculiar 03fg-like or "super-Chandrasekhar" SN 2022pul revealed a dust continuum well fit by a blackbody at $T \approx 500$ K (M. R. Siebert et al. 2024). The SN remnants (SNRs) Tycho and Kepler (both predicted to have been normal SNe Ia) show evidence of dust emission, though their dust masses may be consistent with that which would be collected in the interstellar medium (ISM) as the SN ejecta expand (H. L. Gomez et al. 2012). T. Court et al. (2026) sampled Type Ia SNRs and determined that nearly half show bulk ejecta profiles consistent with CSM interaction beyond what is expected from the ISM alone. Whether normal SNe Ia can produce or heat detectable dust on $\sim$100 days timescales, corresponding to nebular epochs, remains an open question that JWST can address.

Here we present two epochs of contemporaneous optical + NIR + MIR nebular spectroscopy of the normal Type Ia SN 2023qov obtained with ground-based facilities and JWST. We report a clear detection of a cooling dust continuum that is consistent with emission from warm, carbonaceous circumstellar dust. Moreover, we present early-time light-curve modeling and velocity measurements to investigate progenitor and explosion scenarios, comparing against other well-studied regular SNe Ia. SN 2023qov is the fastest-declining normal SN Ia of the published JWST sample so far and thus provides the opportunity to test the nebular properties of fast-declining but otherwise normal SNe Ia. Section 2 presents our ground-based and JWST observations of SN 2023qov. In Section 3, we model the early light curves, compute a luminosity distance, and compare color and Si II velocities to other SNe Ia. In Section 4, we identify and fit the emission lines and dust continuum in the nebular JWST spectra. Our results and the implications of our characterization of SN 2023qov are discussed in Section 5.

2. Observations

2.1. Discovery and Classification

SN 2023qov (Figure 1) was discovered by the Asteroid Terrestrial-impact Last Alert System (ATLAS) sky survey on 2023 August 23 at 04:46:25 UTC at J2000 coordinates of $\alpha = 21^{\mathrm{hr}}12^{\mathrm{m}}02\overset{\mathrm{s}}{.}036$ and $\delta = -49°15'18\overset{''}{.}07$ (J. L. Tonry et al. 2018; A. Aamer et al. 2023). It was found at a brightness of 17.51 ± 0.03 mag in the ATLAS *c* band, with a last nondetection four nights prior (2023 August 19) at a lower limit of 19.28 mag. The SN has an angular separation of $142\overset{''}{.}2$ from the center of its host galaxy NGC 7029 (redshift $z = 0.00947$; R. L. C. Ogando et al. 2008); based on our calculated distance (Section 3.2), this corresponds to a projected physical separation of $\sim$28 kpc. E. Padilla Gonzalez et al. (2023) classified SN 2023qov to be a normal SN Ia using the Supernova Identification (SNID) classification software (S. Blondin & J. L. Tonry 2007).

2.2. Photometry

Following the discovery of SN 2023qov, extensive multi-wavelength, photometric follow-up observations were triggered by the Las Cumbres Observatory network via the Global Supernova Project in the *BgVri* filters, reduced via the LCOGTsnpipe pipeline.[41] Additional imaging by ATLAS contributed a well-sampled light curve in the *oc* bands (Figure 2).

2.3. Ground-based Spectroscopy

21 spectra were obtained with the FLOYDS spectrometer (D. J. Sand et al. 2011) on Las Cumbres Observatory's Faulkes Telescope South (FTS) at a high cadence as part of optical follow-up observations with the Global Supernova Project. They were reduced using the FLOYDS reduction pipeline (S. Valenti et al. 2014). The earliest spectrum taken 13.4 days

[41] https://github.com/LCOGT/lcogtsnpipe

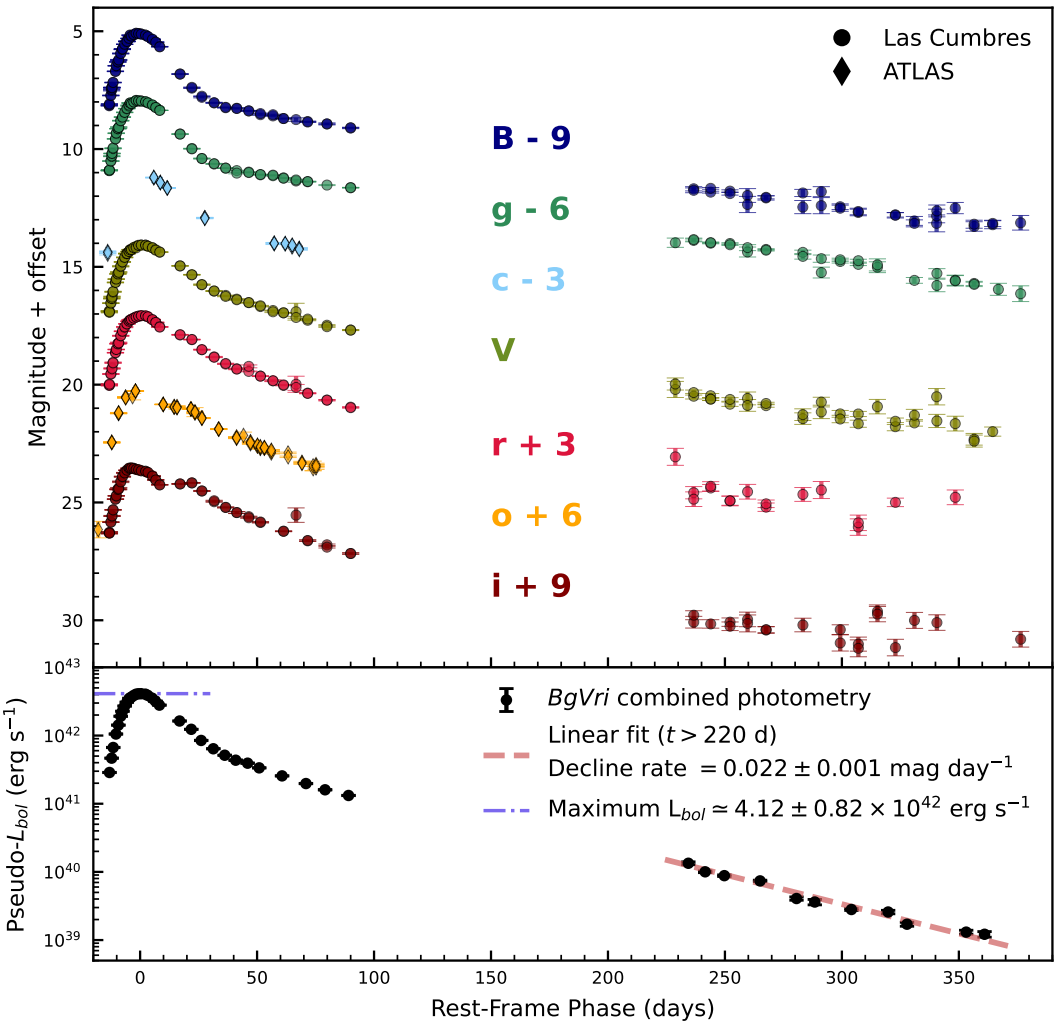


Figure 2. Top: Bessel *BV*- and Sloan Digital Sky Survey (SDSS) *gri*-band photometry of SN 2023qov from Las Cumbres Observatory and ATLAS *oc*-band photometry. The light curve is shown relative to the *B*-band maximum light. Apparent magnitudes are corrected for line-of-sight Milky Way dust extinction. Bottom: the pseudobolometric light curve, combining the *BgVri* bands with the built-in `SNooPy` bolometric light-curve routine (see Section 3.1).
(The data used to create this figure are available in the online article.)

premaximum was used to classify the object (E. Padilla Gonzalez et al. 2023).

Integral field spectroscopic observations of 2023qov, covering seven epochs between 2023 August 25 and 2023 October 21 (UTC dates are used throughout this paper), were obtained with the Wide Field Spectrograph (WiFeS; M. Dopita et al. 2007, 2010) on the Australian National University (ANU) 2.3 m telescope. The observations were done with the B3000 and R3000 gratings in the blue and red arms, respectively, and the X570 dichroic. The data were taken in the Nod-and-Shuffle mode. The data were processed with version 2.0.0 of the PyWiFeS data-reduction pipeline and used standard calibrations to remove instrumental effects and telluric features. The SN flux was then extracted from red and blue data cubes, and the resulting 1D spectra from the two arms were spliced together to form a spectrum covering the 3400–9500 Å wavelength range at a spectral resolution of about 3000.

We obtained seven spectra of SN 2023qov with the Robert Stobie Spectrograph (RSS; M. P. Smith et al. 2006) on the Southern African Large Telescope (SALT), reduced via a custom Pyraf-based reduction pipeline built with standard Pyraf (Science Software Branch at STScI 2012) spectral reduction routines and the `PySALT` package (S. M. Crawford et al. 2010). The reduction included the removal of the host-galaxy lines and continuum, cosmic rays, and telluric absorption. These data ranged from 1.7 days premaximum (2023 September 3) to 281.3 days postmaximum (2024 June 14).

On 2024 June 3 and 2024 September 2, we acquired spectra with the Low Resolution Imaging Spectrometer (LRIS; J. B. Oke et al. 1995) on the 10 m Keck I telescope at the W. M. Keck Observatory. These observations utilized the 1″ slit, the D560 dichroic, the 600/4000 grism, and the 400/8500 grating. This instrument configuration produced a combined wavelength range of ∼3200–10200 Å and a spectral resolving power of $R = \lambda/\Delta\lambda \approx 900$. LRIS has an atmospheric dispersion corrector; nevertheless, to further minimize slit losses caused by atmospheric dispersion (A. V. Filippenko 1982), the slit was oriented at or near the parallactic angle. The LRIS spectra were reduced with the LPipe data-reduction pipeline (D. A. Perley 2019).

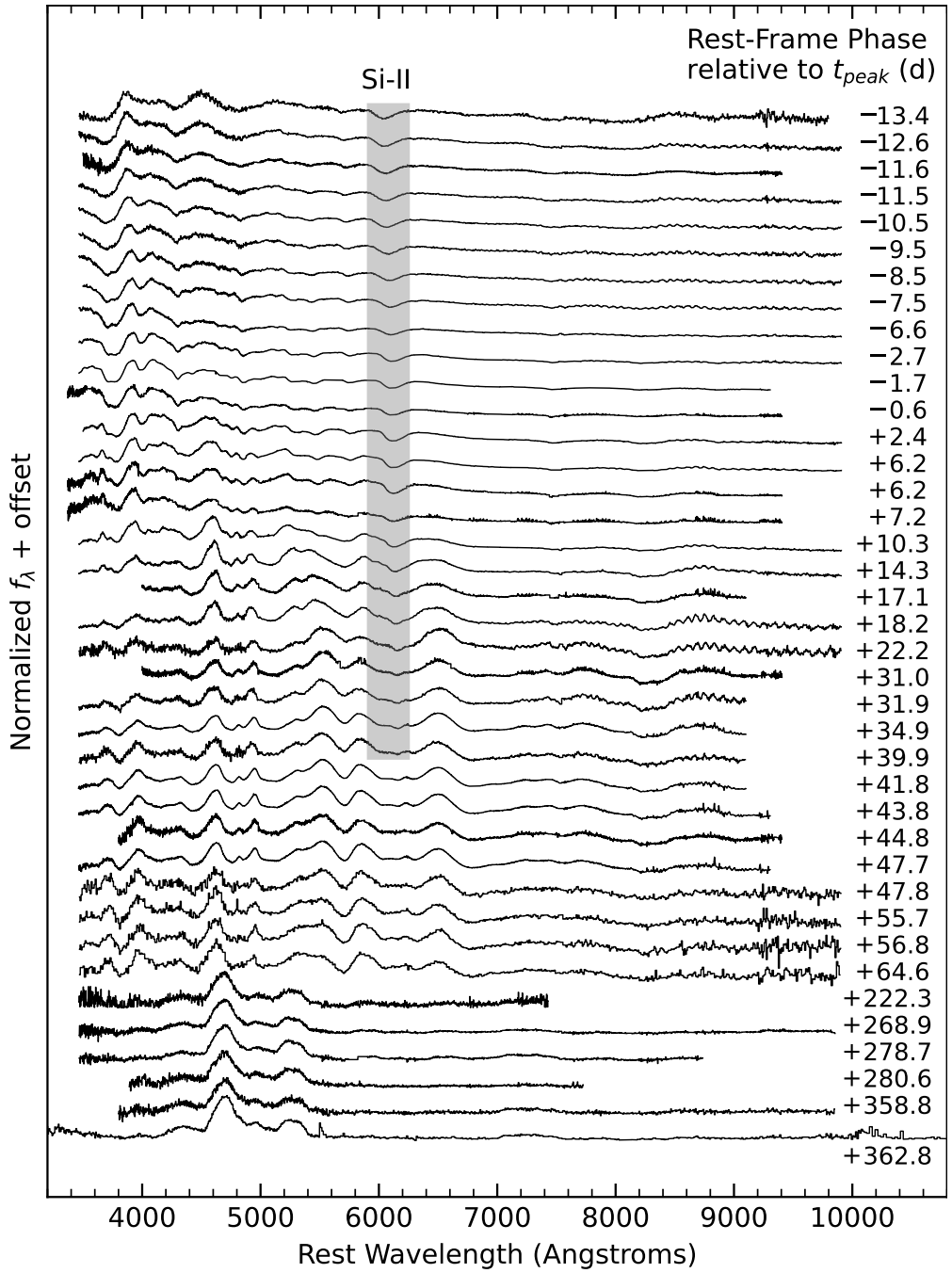


Figure 3. Spectral time series of SN 2023qov, with scaled flux density and wavelength in the rest frame. The spectra are labeled by rest-frame phase relative to the *B*-band peak. The Si II λ6355 absorption feature is highlighted in the early spectra. The full list of observations is presented in Table 1.
(The data used to create this figure are available in the online article.)

Another Keck/LRIS spectrum was obtained on 2024 June 13. To reduce it, we used the `UCSC Spectral Pipeline`[42] (M. R. Siebert et al. 2020), a custom data-reduction pipeline based on procedures outlined by R. J. Foley et al. (2003), J. M. Silverman et al. (2012), and references therein. The 2D spectra were bias corrected, flat-field corrected, adjusted for varying gains across different chips and amplifiers, and trimmed. The spectra were wavelength calibrated using internal comparison-lamp spectra with linear shifts applied by cross-correlating the observed night-sky lines in each spectrum to a master night-sky spectrum. We combine the sides by scaling one spectrum to match the flux of the other in the overlap region and use their error spectra to correctly weight the spectra when combining. More details of this process are discussed elsewhere (R. J. Foley et al. 2003; J. M. Silverman et al. 2012; M. R. Siebert et al. 2020).

A total of seven Very Large Telescope (VLT) XSHOOTER spectra were obtained between 2024 September 6 and 2024 September 9, each with a total integration time of 2400 s split into a 4 × 600 s ABBA nodding cycle. We used a 2 × 2 spectral and spatial binning (slow readout mode) for the UVB and VIS CCDs. To match the requested 1″ seeing, we used

[42] https://github.com/msiebert1/UCSC_spectral_pipeline

Table 1
Log of Spectroscopic Observations

Date (UTC)	MJD	Phase (days)	Telescope/Instrument
2023-08-23	60179.7	−13.4	FTS/FLOYDS
2023-08-24	60180.5	−12.6	FTS/FLOYDS
2023-08-25	60181.5	−11.5	ANU 2.3 m/WiFeS
2023-08-25	60181.6	−11.5	FTS/FLOYDS
2023-08-26	60182.6	−10.5	FTS/FLOYDS
2023-08-27	60183.6	−9.5	FTS/FLOYDS
2023-08-28	60184.6	−8.5	FTS/FLOYDS
2023-08-29	60185.6	−7.5	FTS/FLOYDS
2023-08-30	60186.5	−6.6	FTS/FLOYDS
2023-09-03	60190.4	−2.7	FTS/FLOYDS
2023-09-03	60191.5	−1.7	SALT/RSS
2023-09-05	60192.6	−0.6	ANU 2.3 m/WiFeS
2023-09-08	60195.6	+2.4	FTS/FLOYDS
2023-09-12	60199.4	+6.2	FTS/FLOYDS
2023-09-12	60199.5	+6.2	ANU 2.3 m/WiFeS
2023-09-13	60200.5	+7.2	ANU 2.3 m/WiFeS
2023-09-16	60203.5	+10.3	FTS/FLOYDS
2023-09-20	60207.6	+14.3	FTS/FLOYDS
2023-09-23	60210.4	+17.1	ANU 2.3 m/WiFeS
2023-09-24	60211.5	+18.2	FTS/FLOYDS
2023-09-28	60215.6	+22.2	FTS/FLOYDS
2023-10-07	60224.4	+31.0	ANU 2.3 m/WiFeS
2023-10-08	60225.4	+31.9	FTS/FLOYDS
2023-10-10	60228.4	+34.9	SALT/RSS
2023-10-16	60233.4	+39.9	FTS/FLOYDS
2023-10-17	60235.4	+41.8	SALT/RSS
2023-10-19	60237.4	+43.8	SALT/RSS
2023-10-21	60238.4	+44.8	ANU 2.3 m/WiFeS
2023-10-23	60241.4	+47.7	SALT/RSS
2023-10-24	60241.4	+47.8	FTS/FLOYDS
2023-11-01	60249.4	+55.7	FTS/FLOYDS
2023-11-02	60250.5	+56.8	FTS/FLOYDS
2023-11-10	60258.4	+64.6	FTS/FLOYDS
2024-04-17	60417.6	+222.3	SALT/RSS
2024-06-03	60464.6	+268.9	Keck/LRIS
2024-06-10	60471.4	+275.6	JWST/NIRSpec+MIRI
2024-06-13	60474.6	+278.7	Keck/LRIS
2024-06-14	60476.5	+280.6	SALT/RSS
2024-09-02	60556.0	+358.8	Keck/LRIS
2024-09-05	60559.4	+362.7	JWST/NIRSpec+MIRI
2024-09-08	60561.0	+362.8	VLT/XShooter

Note. Phase in the rest frame, relative to the time of peak B-band brightness.

slits of 1″, 0.″9, and 0.″9 for the UVB, VIS, and NIR arms, respectively. The spectra were reduced using the `XSHOOTER` pipeline v3.6.8 via the EsoReflex environment (W. Freudling et al. 2013). The final spectrum corresponds to a median-combined version of the seven individual spectra. The full ground-based spectral time series is shown in Figure 3 and listed in Table 1.

2.4. JWST Observations

We present NIR+MIR JWST spectra of SN 2023qov at +276 and +363 days in Figure 4. Observations were obtained with the Near Infrared Spectrograph (NIRSpec) in the Fixed Slit Spectroscopy (S. M. Birkmann et al. 2022; P. Jakobsen et al. 2022; J. Rigby et al. 2023) mode with the PRISM, and the Mid Infrared Instrument (MIRI) in the Low Resolution Spectroscopy (S. Kendrew et al. 2015, 2016; J. Rigby et al. 2023) mode, on 2024 June 10 and 2024 September 5 through program GO-4516 (PI: S. W. Jha; S. W. Jha et al. 2024).

The data were reduced using the publicly available JWST reduction pipeline (H. Bushouse et al. 2022) for standard reduction procedures, including bias and dark subtraction, background subtraction, flat-field correction, wavelength calibration, flux calibration, rectification, outlier detection, resampling, and spectral extraction. Inspection of the 2D spectral images and the extracted 1D spectra available on the Mikulski Archive for Space Telescopes (MAST)[43] indicates that the automated reductions are of high quality and further improvements to the data reduction are not necessary.

Table 2
SALT2 Parameters for SN 2023qov, SN 1994D, SN 2022aaiq, SN 2024gy, and SN 2021aefx

	m_B (peak)	x_1	c
SN 2023qov	+13.830 ± 0.018	−1.715 ± 0.014	−0.049 ± 0.016
SN 1994D	+11.704 ± 0.027	−1.627 ± 0.025	−0.069 ± 0.024
SN 2022aaiq	+13.327 ± 0.018	−0.294 ± 0.031	−0.133 ± 0.017
SN 2024gy	+12.916 ± 0.021	+0.063 ± 0.012	+0.273 ± 0.019
SN 2021aefx	+11.980 ± 0.002	+0.292 ± 0.009	+0.013 ± 0.001

3. Photospheric Phase

3.1. Light Curves

The photometric data for SN 2023qov are modeled with fits to the Spectral Adaptive Light curve Template (SALT) (J. Guy et al. 2005, 2007). Specifically, we use the SALT2 model, which has been shown to have better matches to premaximum photometry when compared to the more recently trained SALT3 (M. Rigault et al. 2025). We perform these fits through the `SNCosmo` package (K. Barbary et al. 2016). The SALT2 model fits SN Ia light curves across each band with three primary parameters: x_o, x_1, and c. A smaller value of x_1 indicates faster evolution; c describes the SN color and is parameterized as $c = (B - V)_{\max} - \langle B - V \rangle$.

From the SALT2 fits, we define a peak B-band magnitude:

$$m_B = -2.5 \log(x_0) + 10.5, \quad (1)$$

where by convention $m_B = 10.5$ mag corresponds to $x_0 = 1$ (W. D. Kenworthy et al. 2021).

Applying the color and stretch corrections directly to the distance modulus yields

$$\mu_{\rm obs} = m_B + \alpha\, x_1 - \beta\, c - M_B, \quad (2)$$

where $\mu_{\rm obs}$ represents the inferred distance modulus, and α, β, and M_B are parameters that are obtained by performing a cosmological fit with a full sample of SNe Ia.

We correct for Milky Way dust extinction in our SALT2 model fit by assuming a Milky Way $R_V = 3.1$ and setting $E_{\rm MW}(B - V) = 0.033$ mag, which is the value along the line of sight obtained from the dust maps of E. M. Schlegel (1990), recalibrated by E. F. Schlafly & D. P. Finkbeiner (2011). As SN 2023qov is well separated from its elliptical host (NGC 70290), we expect little host-galaxy extinction contribution, so the SALT2 color parameter (c) is likely representative of the

[43] https://mast.stsci.edu/portal/Mashup/Clients/Mast/Portal.html

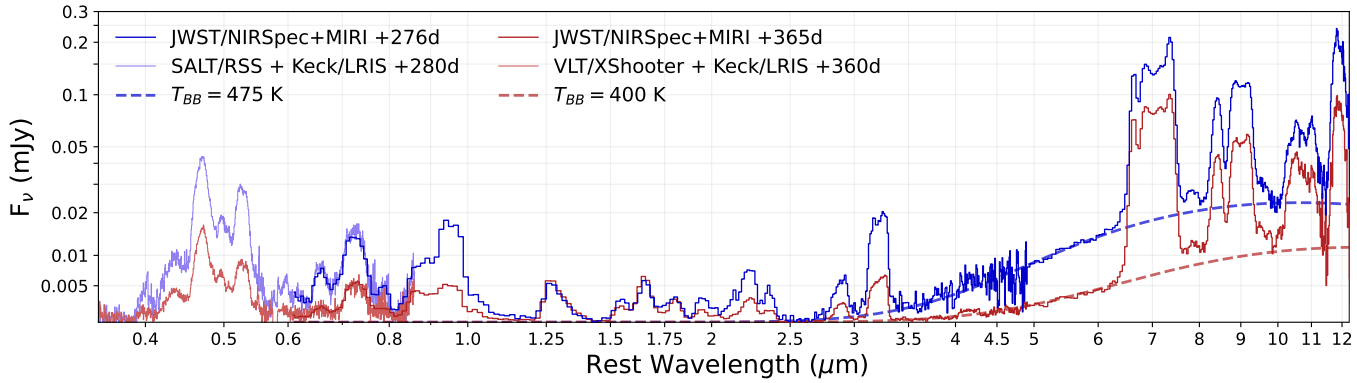


Figure 4. Optical and NIR/MIR spectra of SN 2023qov taken at +276 (brighter spectra, shades of blue) and +363 (fainter spectra, shades of red) days since peak brightness. The dashed lines show a fading blackbody at $T = 475$ K (blue) and $T = 400$ K (red). These blackbody fits are discussed in Section 4.

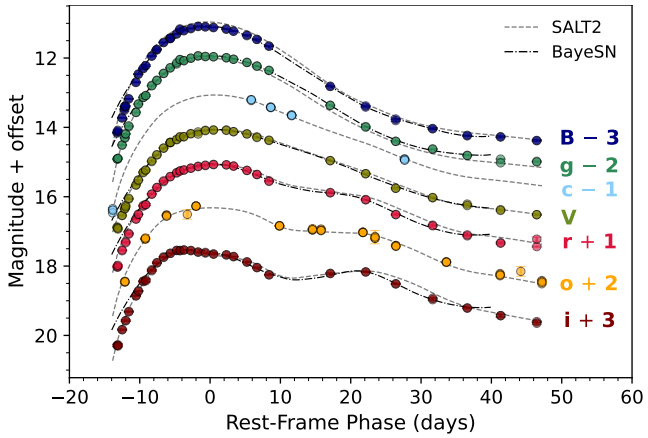


Figure 5. Early light-curve photometry fit with the SALT2 and BayeSN models. SALT2 is signified by the dashed gray line, and BayeSN by the dashed–dotted black line. BayeSN is cut off beyond 40 days and before −14 days as it is best trained to fit the peak features of the light curve, and it does better than SALT2 in that range. BayeSN does not have built-in bandpasses for ATLAS *o* and *c*.

intrinsic color of SN 2023qov (as well as the potential contribution from its CSM, discussed in Section 4.1).

The SALT2 fit of SN 2023qov (Figure 5) shows a peak *B*-band magnitude of 13.830 ± 0.018 at $t_0 = 60193.186 \pm 0.015$ MJD. SN 2023qov has a fast-declining light curve with $x_1 = -1.715 \pm 0.014$, and is slightly red at $c = -0.049 \pm 0.016$. Table 2 compares these results with those of four other regular SNe Ia. SN 1994D is a close match in color, decline rate, and host separation, and the others are sampled with JWST.

We also fit SN 2023qov with `BayeSN`, a hierarchical Bayesian SN Ia light-curve-fitting code (K. S. Mandel et al. 2022). BayeSN differs from the SALT2 model in that it treats host-galaxy dust and intrinsic SN spectral energy distribution (SED) variations separately, instead of combining the two properties into a single color parameter. It thus fits for the *V*-band extinction (A_V) directly and marginalizes over the covariances of the SN SED residuals to capture both of these physically distinct factors simultaneously. BayeSN also fits for the distance modulus directly, assuming a fiducial cosmology from the results of A. G. Riess et al. (2016).

Additionally, we employ `Supernova Python` (`SNooPy`) to fit the light curve of SN 2023qov (C. R. Burns et al. 2011, 2014). M. M. Phillips et al. (1999) define the traditional $\Delta m_{15}(B)$ as the decrease in *B*-band magnitude from peak brightness to +15 rest-frame days. We determine this to be $\Delta m_{15}(B) = 1.47 \pm 0.05$ mag via the BayeSN *B*-band fit. `SNooPy` defines the Δm_{15} parameter in its *EBV Model 2*,[44] from which we determine $\Delta m_{15} = 1.458 \pm 0.063$ mag and the host $E(B - V) = -0.042 \pm 0.064$ mag, consistent with our assumption of minimal host contribution. This Δm_{15} is slightly systematically different from $\Delta m_{15}(B)$ (C. R. Burns et al. 2011), although we note that they are very similar for SN 2023qov. C. R. Burns et al. (2014) introduce the color-stretch parameter s_{BV}, which reduces sensitivity to reddening by relating t_0 to the $B - V$ color-curve peak. Fitting the same *EBV_model2* with instead the s_{BV} parameter, we find $s_{\rm BV} = 0.759 \pm 0.032$, and again a near-zero host reddening of $E(B - V) = -0.014 \pm 0.063$ mag. Using the relations between $s_{\rm BV}$, Δm_{15}, and the SALT2 x_1 parameter, we verify the consistency of these three results.

`SNooPy` includes a built-in bolometric light-curve routine, for which we adopt the "direct" method. This method integrates the observed bandpasses to estimate fluxes, then fits blackbodies to predict the IR and UV contributions. The procedure yields a pseudobolometric light curve, shown in Figure 2 (from here on, we succinctly refer to it as a "bolometric" light curve). We estimate uncertainties by perturbing each photometric point according to its reported uncertainty and recomputing the bolometric light curve 500 times. This represents a total optical contribution to the bolometric luminosity, as the IR echo discussed in Section 4.1 is not taken into account in this estimate. We use SciPy's `curve_fit` (C. R. Harris et al. 2020; P. Virtanen et al. 2020) to fit a line to the late-time data, which results in a predicted optical bolometric magnitude decline of 0.022 ± 0.001 mag day^{-1}. The peak of the light curve is fit with a spline to determine a peak optical luminosity of $L_{\rm bol} = 4.12 \pm 0.82 \times 10^{42}$ erg s^{-1}. We determine the uncertainty by bootstrapping 2000 times, and assume an additional systematic error of ∼15% owing to the lack of UV or NIR data. Using Arnett's rule (W. D. Arnett 1982; see Equation (5) of S. Dhawan et al. 2016) and this luminosity estimate, we predict a ^{56}Ni mass of $M_{56} = 0.21 \pm 0.04\,M_\odot$. This is quite different from its SALT2 analog SN 1994D, which is predicted to have $M_{56} \approx 0.6$–$0.8\,M_\odot$ (P. Höflich 1995; E. Cappellaro et al. 1997).

[44] https://users.obs.carnegiescience.edu/cburns/SNooPyDocs/html/models.html

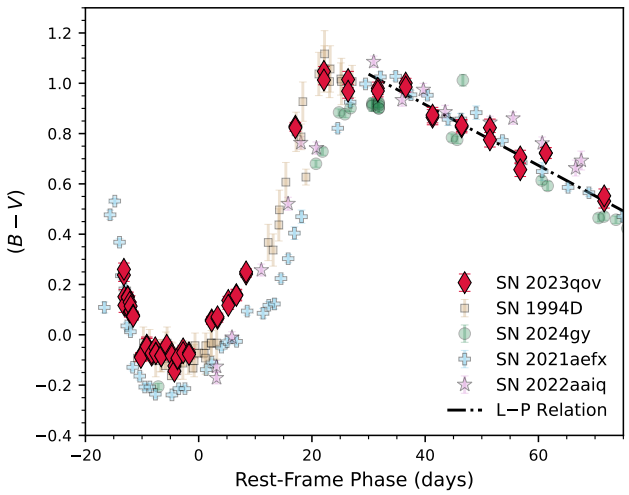


Figure 6. The $B - V$ color curve of SN 2023qov compared with SNe Ia 1994D (M. Hicken et al. 2009), 2021aefx (G. Hosseinzadeh et al. 2023), 2022aaiq, and 2024gy (L. A. Kwok et al. 2026), corrected for Milky Way dust extinction $E_{\rm MW}(B-V)$. The rest-frame phase is relative to the time of B maximum. The line shows the Lira–Phillips relation (P. Lira 1996; M. M. Phillips et al. 1999), where $t(V_{\rm max}) \approx 60194.7 \pm 0.1$, or 1.5 days after $t(B_{\rm max})$.

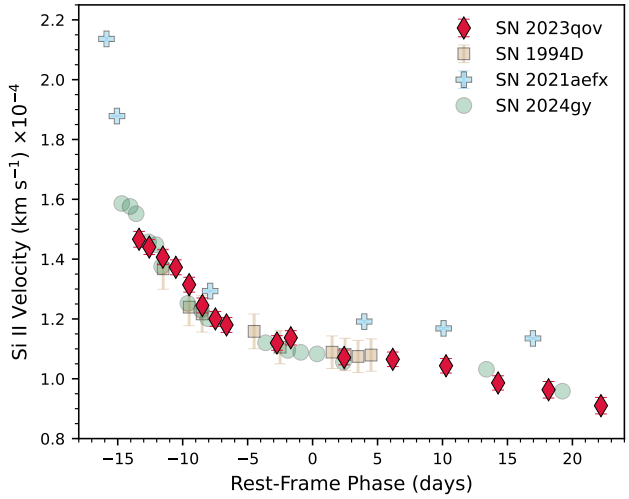


Figure 7. The Si II ($\lambda_{\rm rest} = 6355$ Å) velocity of SN 2023qov in early phases compared against SN 1994D (F. Patat et al. 1996), SN 2021aefx (C. Ashall et al. 2022), and SN 2024gy (L. Li et al. 2026). We do not include SN 2022aaiq as a comparison object owing to a lack of early-time spectra.

3.2. Distance

We recover a distance modulus from our BayeSN fit of $\mu_{\rm BayeSN} = 32.78 \pm 0.11$ mag, corresponding to a luminosity distance of 36.0 ± 1.8 Mpc. As mentioned, BayeSN also fits for the selective V-band host dust extinction, which in this case is $A_V = 0.12 \pm 0.05$ mag. We note that this value is consistent with 0 mag to within 2.4σ, which agrees with the result of `SNooPy` and our assumption of little line-of-sight dust given its isolated environment.

The distance modulus derived from the SALT2 method in Equation 2 requires assumed fit parameters for decline-rate correction α, color correction β, and fiducial B-band absolute magnitude M_B. Recently, it has been shown that the optimal decline-rate correction parameter (α) changes depending on whether the SN Ia is fast declining or slow declining (P. Garnavich et al. 2023; C. Larison et al. 2024; M. Ginolin et al. 2025). Therefore, to make an accurate correction owing to the decline rate, we fit these standardization parameters using the sample from C. Larison et al. (2024), with only the $z < 0.06$ (to avoid Malmquist bias) and fast-evolving ($x_1 < -1$) SNe Ia selected, using the same fiducial cosmology as our BayeSN model to ensure an accurate comparison. For this fit, we employ a Markov Chain Monte Carlo (MCMC) technique, which also fits for an intrinsic scatter parameter $\sigma_{\rm int}$, which captures the variations of the SNe Ia away from the assumed cosmology after standardization. The values we recover for our fit parameters are $\alpha = 0.167 \pm 0.033$, $\beta = 2.539 \pm 0.156$, $M_B = -19.115 \pm 0.064$, and $\sigma_{\rm int} = 0.156 \pm 0.012$. With this standardization, we find a distance modulus of $\mu_{\rm SALT2} = 32.78$ mag, with a contribution to the uncertainty from light-curve fitting of 0.05 mag. With this measurement, the SALT2 and BayeSN values are in excellent agreement. Such a test between the two methods was also performed by M. J. B. Newman et al. (2026) on six regular SNe Ia, from which they found similar agreement between the BayeSN and SALT2 methods when making similar selection cuts on the SN Ia cosmological samples.

We note that the BayeSN fit to the light curve of SN 2023qov has a lower reduced χ^2 than the SALT2 fit (both shown in Figure 5), with reduced χ^2 values of 1.9 and 2.7 for the BayeSN and SALT2 fits, respectively. Therefore, we recommend using the final distance recovered from BayeSN, with full statistical uncertainty as stated above.

3.3. Colors and Velocities

Figure 6 shows the $B - V$ color of SN 2023qov, corrected for Milky Way extinction from the NASA/IPAC Extragalactic Database (NED) extinction calculator.[45] The color was calculated by interpolating and subtracting the B- and V-band magnitudes. Similar to the comparison SNe Ia, SN 2023qov is blue at maximum. Early emission shows little blue excess compared to SN 2021aefx, though both show some especially defined "infant-reddening" within the first few days. SN 2023qov's color is similar to its SALT2 match, SN 1994D. The B and V light curves have a gap at 10–20 days for SN 2023qov. Beyond 30 days, SN 2023qov begins to better match the color of the comparison SNe, as it falls along the Lira–Phillips relation (P. Lira 1996; M. M. Phillips et al. 1999).

With the spectra collected before 25 days postexplosion, we measure the Si II absorption-line minimum ($\lambda_{\rm rest} = 6355$ Å) by fitting a single Gaussian curve with a linear component to correct for the underlying photospheric continuum with `curve_fit` from `NumPy` (C. R. Harris et al. 2020). Adopting the resulting parameters as initial values, we use the Python package `emcee` (D. Foreman-Mackey et al. 2013) to determine the best fit and uncertainty via the Monte Carlo method. From this result we calculate the Si II velocity at maximum absorption over the first 25 days. Figure 7 compares the calculated Si II velocity curve against other SNe Ia. SN 2023qov is similar in velocity to most comparisons, and can be put into the normal-velocity subclass according to the classification scheme proposed by X. Wang et al. (2009). The outlier is SN 2021aefx, and SN 2023qov is again similar to SN 1994D. Both of these comparisons also fit well with strong, multicomponent, high-velocity Si II models (see

[45] https://ned.ipac.caltech.edu/extinction_calculator

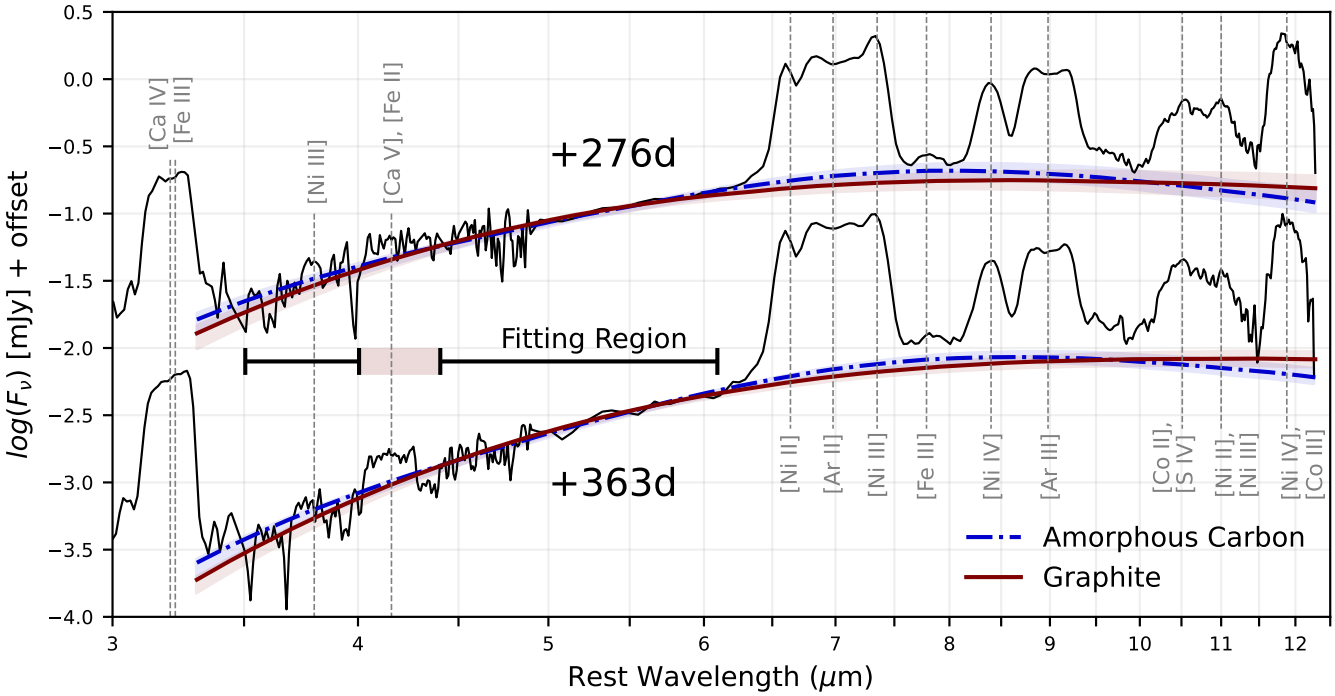


Figure 8. Two epochs of JWST spectra fit against carbonaceous dust models from C. Jäger et al. (1998) (dashed–dotted line) and B. T. Draine & H. M. Lee (1984) (solid line), both with 2σ model uncertainties overplotted. The region 3.5–6 μm was used to fit the models, with the blended [Ca V]/[Fe II] 4.2 μm feature cut out (denoted with the red shaded region).

Table 3
Ejecta Radii and Dust Parameters for the Blackbody, Graphite, and Amorphous Carbon Models over Both Nebular Epochs

Epoch	$r_{\rm ejecta}$ (lt-yr)	$T_{\rm BB}$ (K)	$r_{\rm BB}$ (lt-yr)	$M_{\rm Gra}$ ($M_\odot$)	$T_{\rm Gra}$ (K)	$M_{\rm AMC}$ ($M_\odot$)	$T_{\rm AMC}$ (K)
+276 days	$\sim 3 \times 10^{-2}$	476 ± 7	$(7.1 \pm 0.2) \times 10^{-3}$	$3.51^{+0.71}_{-0.60} \times 10^{-4}$	375 ± 9	$2.09^{+0.39}_{-0.32} \times 10^{-4}$	419 ± 10
+363 days	$\sim 4 \times 10^{-2}$	397 ± 5	$(6.5 \pm 0.2) \times 10^{-3}$	$3.09^{+0.41}_{-0.34} \times 10^{-4}$	325 ± 5	$1.66^{+0.20}_{-0.19} \times 10^{-4}$	362 ± 6

J. M. Silverman et al. 2015), though the data here are single Gaussian fits, likely dominated by the photospheric velocity.

4. Nebular Phase

4.1. Dust Emission

The most striking feature of the MIR spectroscopy of SN 2023qov is the additional flux continuum that can be seen starting at 3.5 μm (see Figure 4), which is indicative of IR reemission of light absorbed from the SN by circumstellar dust. We do not see evidence of silicate dust or polycyclic aromatic hydrocarbons (PAHs) in the spectra (B. T. Draine & H. M. Lee 1984; B. T. Draine 2011), nor is there evidence of any molecules (such as CO or SiO). As an initial characterization, we fit a blackbody model to each JWST epoch in the range 3.5–6.4 μm, which is free from strong emission lines. We bootstrap the datasets 5000 times assuming a 10% uncertainty. For epoch 1 (+276 days), we measure a blackbody temperature, $T_{\rm BB,Ep1} = 476 \pm 7$ K, and for epoch 2 (+363 days), $T_{\rm BB,Ep2} = 397 \pm 5$ K. Because this is not a comprehensive dust model, we expect the uncertainties are underestimated; we show example blackbody fits at $T = 475$ K and $T = 400$ K for epochs 1 and 2, respectively, in Figure 4. Nevertheless, we see clear support for a cooling temperature of $\sim$80 K in 90 days. Integrating the total blackbody flux we calculate a blackbody radius $r_{\rm BB} = \sqrt{L_{\rm BB}/(4\pi\sigma T_{\rm BB}^4)}$, given in Table 3. Because the blackbody model assumes the dust is in an optically thick spherical shell, the resulting radii are only a lower limit to the physical size. Indeed, our calculated blackbody radii are within the expected ejecta radii at both epochs (taking $r_{\rm ejecta} \approx v_{\rm Bmax} t$ and $v_{\rm Bmax} \approx 11,000\,{\rm km\,s^{-1}}$, the results are listed in Table 3), an unlikely region for preexisting dust to survive. This implies that the dust is either optically thin, not spherically distributed, or both. We do not see evidence of dust formation (e.g., through molecular lines; see Section 5). For our subsequent analysis, we assume the dust is optically thin and at a larger physical radius.

To better estimate the dust mass and temperature giving rise to this MIR continuum, we fit two optically thin carbonaceous dust models, shown in Figure 8. We fit a similar region to the blackbody fits, cutting out the 4.21 μm [Ca V]/[Fe II] feature. To determine uncertainties, we bootstrap the datasets 5000 times for each model and epoch. In order to calculate flux as a function of wavelength, we employ an optically thin dust-emission model:

$$F_\nu = \frac{\kappa M}{d_{SN}^2} B_\lambda(\lambda, T). \quad (3)$$

We take $d_{\rm SN} \approx 36.0$ Mpc (Section 4.1), and $B_\lambda(\lambda, T)$ is the Planck blackbody function. The final parameter is the opacity:

$$\kappa = \frac{3}{4\rho a} Q_{\rm abs}(\lambda), \quad (4)$$

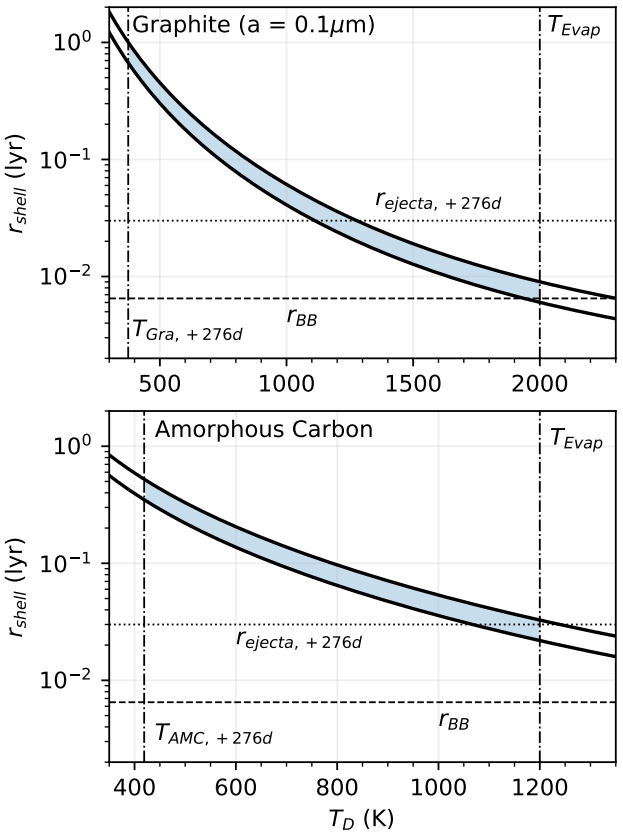


Figure 9. Possible shell radii ($r_{\rm shell}$) of CSM around SN 2023qov, plotted against the maximum continuum temperature to which the dust is heated $T_{\rm D}$, from a spherical dust IR echo model (Section 4.2). Here, $T_{\rm Gra/AMC,+276d}$ is our measured temperature for both dust species (Section 4.1), corresponding to a lower limit on $T_{\rm D}$, and $T_{\rm Evap}$ is the maximum temperature allowed for the species of dust. The blackbody radii are $r_{\rm BB}$, determined in Section 4.1. We plot the radii of both species for a range of 2σ of $L_{\rm bol}$, determined in Section 3.1, to account for the uncertainty in the true optical bolometric luminosity of SN 2023qov.

where $Q_{\rm abs}$ is the absorption efficiency, ρ is the density of the grain material, and a is the average grain radius. We apply the optical graphite absorption efficiency model from B. T. Draine & H. M. Lee (1984), assuming a density of 2.24 g cm^{-3} and an average grain size of 0.1 μm, representative of standard astronomical graphitic dust and commonly adopted in light-echo and circumstellar dust calculations (B. T. Draine & A. Li 2007). The amorphous carbon (AMC) model from C. Jäger et al. (1998) is also used, giving a model for $Q_{\rm abs}/a$, and we assume a density of 1.85 g cm^{-3} (F. Rouleau & P. G. Martin 1991; V. G. Zubko et al. 1996). Varying these dust properties has an effect of a factor of a few on the measured dust masses, so the masses should be regarded as an order-of-magnitude estimate. The exact dust parameters do not substantially change our findings. The resulting parameters are shown in Table 3. Both models give consistent, or somewhat decreasing, dust masses across the two epochs.

4.2. Thin Spherical Shell IR Echo Model

To further constrain its properties, we model the dust emission as IR reemission of the optical radiation from the SN, assuming the majority of the initial dust heating occurred from peak brightness. We define $L_{\rm bol}$ as our calculated peak luminosity in the UV and optical (Figure 2). Following a derivation similar to that of O. D. Fox et al. (2010, see their Section 3.3), we assume a thin shell, and balance the radiation absorbed and reemitted by the dust, setting $L_{\rm abs} = L_{\rm D}$, and resulting in an effective shell radius

$$r_{\rm shell}^2 = \frac{3}{64}\frac{L_{\rm bol}}{a\rho\sigma T_{\rm SN}^4}\frac{\int B_\nu(T_{\rm SN})Q_{\rm abs}(\nu)d\nu}{\int B_\nu(T_{\rm D})\kappa(\nu)d\nu}. \quad (5)$$

Here $T_{\rm SN}$ is the effective temperature of the SN at peak brightness, which we estimate as $T_{\rm SN} \approx 10,500$ K by fitting a continuum to the peak optical spectrum. The result does not depend precisely on $T_{\rm SN}$. Also, $T_{\rm D}$ is the maximum temperature to which the dust is heated. We take this to be the temperature at the first epoch for both dust compositions, though this is a lower limit, as the dust temperature may have exceeded this at an earlier epoch than observed. We also note an upper limit of temperatures, at $T_{\rm Evap,\ Gra} \approx 2000$ K and $T_{\rm Evap,\ AMC} \approx 1200$ K, based on estimates of their sublimation temperatures (B. T. Draine 2011; T. D. Blasius et al. 2012). Figure 9 shows the possible radii given these constraints.

We find the upper limits on shell radii of $R_{\rm Gra} < 0.85 \pm 0.22$ lt-yr and $R_{\rm AMC} < 0.44 \pm 0.11$ lt-yr. Uncertainties were estimated by propagating the errors of $T_{\rm D}$ and $L_{\rm bol}$. These results are consistent with the timescale expected of an IR echo owing to CSM within 1 lt-yr of the SN. Declining dust emission is expected to begin once the light from the peak of the SN has passed through the bulk of the dust. Thus, since we see a decline in dust emission at some time $\lesssim$1 yr, we expect the majority of dust to be within or near 1 lt-yr for most geometries (see K. Maeda et al. 2015 and O. D. Fox et al. 2010 for further discussion on the relationship between phase and geometry in IR echos). Higher-cadence MIR sampling of a "dusty" SN Ia like SN 2023qov would allow for the further constraining of dust heating and cooling timescales, as well as their corresponding distances and geometries.

4.3. Emission-line Morphology

To identify nebular emission lines, we follow the predictions of S. Blondin et al. (2023) and the analyses of the other normal SNe Ia SN 2021aefx (L. A. Kwok et al. 2023; C. Ashall et al. 2024), SN 2022aaiq, and SN 2024gy (L. A. Kwok et al. 2026). SN 2023qov shares the same dominant spectral lines with these objects, but there are a few differences. We identify the 7.788 μm feature to be [Fe III] (S. Blondin et al. 2023), which is more clearly present than in other analyses. The flat-topped 4.21 μm feature, only strongly present in the second epoch, appears to be a blended combination of primarily [Ca V] and a possible weak contribution from two distinct [Fe II] lines, though the low signal-to-noise ratio (S/N) in this region makes characterization difficult. The blended feature in the $\sim$10.5 μm region is somewhat distinct in morphology from previous objects, consistent with being blended [S IV], [Co II], [Ni II], and [Ni III] lines, with the [S IV] being especially pronounced.

Following the procedures described by L. A. Kwok et al. (2023, 2024, 2026), we subtract the best-fit blackbody models and fit NIR and MIR emission-line profiles for both epochs. In doing this, we assume the dust is preexisting and thus not impacting the line profiles. We select the dominant emission lines in the 6–12.4 μm region to fit: [Ni II] 6.63, 10.679 μm, [Ar II] 6.985 μm, [Ni III] 7.349, 11.002 μm, [Ni IV] 8.405,

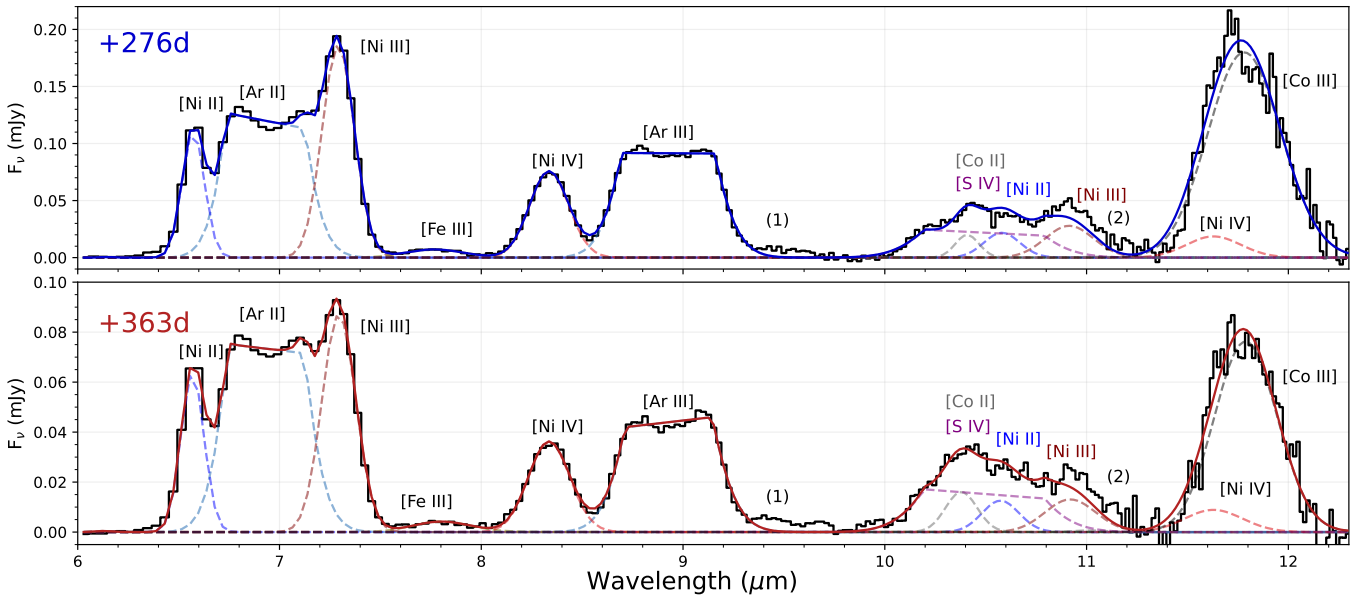


Figure 10. Nebular line fits to the blackbody-subtracted JWST/MIRI spectra (black). The top panel shows epoch 1 (+276 days); the bottom panel shows epoch 2 (+363 days). The less blended features on the left side of the plot are weighted more heavily in the fit, so the lines in the heavily blended 10–11 μm feature are well constrained, with the exemption of [S IV] and [Co II], which do not appear outside of the blended region. Label (1) shows an ambiguous feature with low S/N, which could be various IGEs. Label (2) highlights an ambiguous excess that we attribute to either noise, an underpredicted model relative line strength of [Ni II] (S. Blondin et al. 2023), possible 11.24 μm [Ni V] emission, or some combination of unidentified weak lines. The features are discussed in Section 4.3.

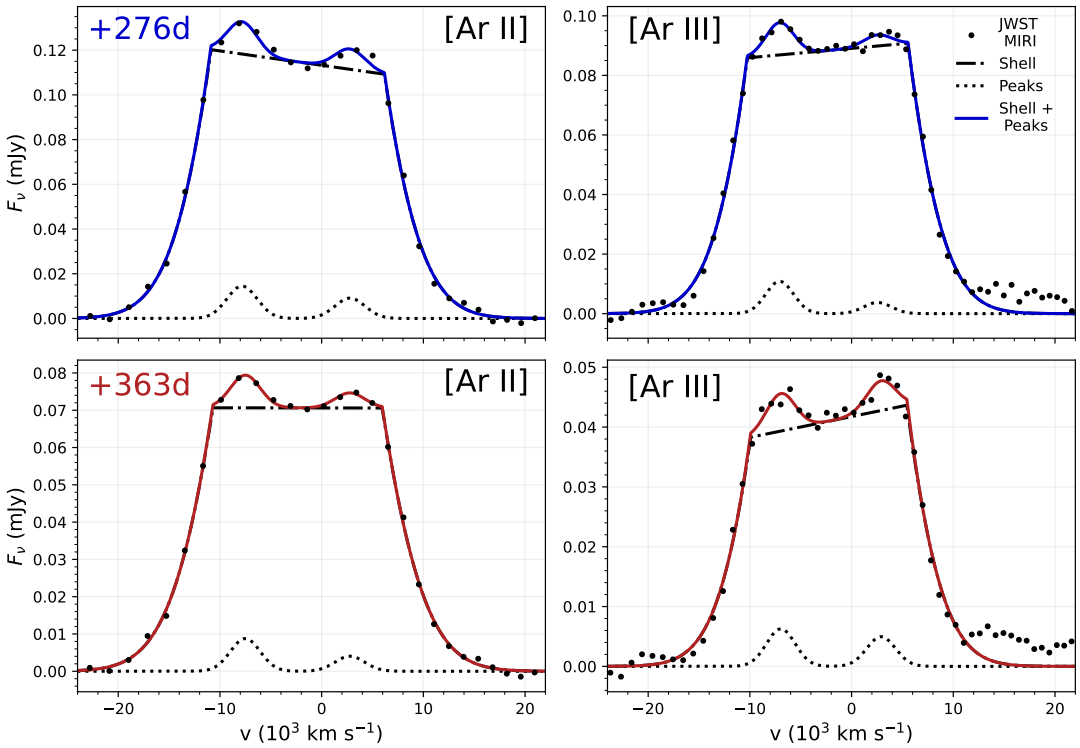


Figure 11. Simple torus model fit of [Ar II] and [Ar III] features marked in Figure 10. The upper panels are from the first epoch (+276 days) and the lower are from the second (+363 days) of JWST/MIRI data of SN 2023qov. The peaks and shell are combined into one model, with the Gaussian contributions constrained to 5%–10% of the amplitude and full width at half-maximum (FWHM) intensity of the shell to constrain degeneracies.

11.723 μm, [Ar III] 8.991 μm, [Co II] 10.521 μm, [S IV] 10.510 μm, and [Co III] 11.888 μm. These are consistent with SN Ia abundance models (e.g., K. Nomoto et al. 1984; F.-K. Thielemann et al. 1986; M. Fink et al. 2010; R. Pakmor et al. 2012; I. R. Seitenzahl et al. 2013) and were also examined in the nebular JWST analyses of other normal SNe Ia. The lines are fit together in order to preserve the relative line strengths between transitions of the same ion from S. Blondin et al. (2023). The region 6–9.4 μm is weighted more heavily in the fit in order to better constrain the blended $\sim$11 μm region. This is done via SciPy's curve_fit *sigma* argument, where the blended region is assumed to have double

Table 4
MIR Line Identification and Fit Parameters for SN 2023qov (Figure 8)

λ_{rest} (μm)	Line	Profile	Best-fit Parameters Epoch 1 (+276 days)	Best-fit Parameters Epoch 2 (+363 days)
6.636, 10.679	[Ni II]	Gaussian	v_{FWHM}: 5.91 ± 0.65, v_{off}^{b}: −2.80 ± 0.26	v_{FWHM}: 6.12 ± 0.55, v_{off}: −2.99 ± 0.24
6.985	[Ar II]	Shell	v_{FWHM}: 20.93 ± 0.99, v_{off}: −2.48 ± 0.31 v_{inner}: 8.39 ± 0.23, v_c: −0.20 ± 0.14	v_{FWHM}: 21.09 ± 0.96, v_{off}: −2.32 ± 0.25 v_{inner}: 8.19 ± 0.25, v_c: −0.10 ± 0.13
7.349, 11.002	[Ni III]	Gaussian	v_{FWHM}: 7.72 ± 0.43, v_{off}: −2.32 ± 0.21	v_{FWHM}: 8.12 ± 0.43, v_{off}: −2.19 ± 0.24
8.405, 11.723	[Ni IV]	Gaussian	v_{FWHM}: 8.20 ± 0.61, v_{off}: −2.42 ± 0.24	v_{FWHM}: 8.71 ± 0.70, v_{off}: −2.42 ± 0.27
8.991	[Ar III]	Shell	v_{FWHM}: 19.73 ± 0.67, v_{off}: −2.20 ± 0.17 v_{inner}: 7.80 ± 0.27, v_c: −0.01 ± 0.15	v_{FWHM}: 18.68 ± 0.77, v_{off}: −1.94 ± 0.19 v_{inner}: 7.25 ± 0.34, v_c: 0.17 ± 0.16
10.510	[S IV]	Shell	v_{FWHM}: 19.44 ± 0.85, v_{off}: −1.00[a] v_{inner}: 8.50[a], v_c: −0.50[a]	v_{FWHM}: 21.26 ± 0.91, v_{off}: −1.00[a] v_{inner}: 8.50[a], v_c: −0.50[a]
10.521	[Co II]	Gaussian	v_{FWHM}: 4.00 ± 2.65, v_{off}: −3.21 ± 0.73	v_{FWHM}: 5.34 ± 1.94, v_{off}: −4.04 ± 0.41
11.888	[Co III]	Gaussian	v_{FWHM}: 10.88 ± 0.19, v_{off}: −2.63 ± 0.08	v_{FWHM}: 9.32 ± 0.22, v_{off}: −2.45 ± 0.09

Notes. The velocities are in units of 10^3 km s^{-1}. In both profiles, v_{off} represents the offset of the central line profile from rest in velocity space. In the shell profile, v_{inner} is a proxy for the width of the "flat-top" and v_c is a proxy for the slope of the "flat-top," the velocity offset center of the shell to the center of emission, with positive (negative) values having positive (negative) slope.
[a] [S IV] v_{FWHM} and v_{inner} are fixed based on the unblended [Ar II] and [Ar III] features; owing to heavy blending, [S IV] and [Co II] are poorly constrained.
[b] The systematic offset in v_{off} for each line is indicative of an off-center explosion, with the epicenter of the explosion being closer to the observer along the line of sight relative to the rest frame.

the uncertainty compared to the unblended region. This also helps to ensure the higher-S/N blueward region of the MIRI spectrum is more strongly influencing the fit.

We fit Gaussian profiles to the Ni and Co lines, while we fit flat-topped profiles with Gaussian wings to the Ar and S lines. The shell model produces an emission line having a boxy, flat-topped shape with Gaussian wings. We primarily select these profiles based on the work of L. A. Kwok et al. (2024), who showed that the line profiles of these IMEs differ from the IGEs that dominate at nebular times, which also aligns with expectations from models involving detonations (e.g., S. Blondin et al. 2023). The fits to the dominant lines are listed in Table 4 and shown in Figure 10.

A notable feature in SN 2023qov is the double-peaked ("horned") nature of the Ar lines (and likely S, though line blending makes the shape uncertain), which are distinct from SN 2021aefx, SN 2022aaiq, and SN 2024gy. This deviation from the "flat-top" resulting from a spherical shell geometry indicates that the emission is somewhat toroidal. C. L. Gerardy et al. (2007) also found double-peaked, ringlike Ar emission in Spitzer MIR spectra of SN 2005df and SN 2003dh, which appear more pronounced than in SN 2023qov.

The toroidal geometry still indicates stratified ejecta with the IMEs located in outer layers, supported by our measured line widths (see Table 4). The IGEs have narrower widths than the IMEs, indicating that they are located closer to the center of the ejecta.

In the overall fit (Figure 10) we employ a shell model for the Ar emission, but to further analyze the structure of these horned line profiles, we fit a shell with two smaller Gaussian contributions to represent the torus, shown in Figure 11. To isolate the Ar lines, we first subtract the neighboring Ni line contributions using the previous fits. We then combine our slanted shell model with two smaller Gaussian peaks. We estimate and constrain the flux amplitude of the Gaussian contributions to be 5%–10% of the amplitude of the shell. This is physically motivated, as the bulk geometry is expected to be shell-like, while the additional Gaussian components are

Table 5
Parameters from Combined Shell and Double Gaussian Fits (Figure 11)

Epoch 1 (+276 days)		
Ion	[Ar II]	[Ar III]
Shell Component		
A_{shell}	0.37 ± 0.01	0.28 ± 0.02
v_{FWHM}	21.23 ± 0.17	19.80 ± 0.24
v_{off}	−2.53 ± 0.04	−2.26 ± 0.05
v_{in}	8.52 ± 0.07	7.90 ± 0.10
v_c	−0.17 ± 0.04	0.09 ± 0.08
Gaussian Components		
A_{blue}	0.015 ± 0.002	0.011 ± 0.003
A_{red}/A_{blue}	0.63 ± 0.24	0.35 ± 0.32
v_{FWHM}	3.50[a]	3.20 ± 0.73
Δv	10.62 ± 0.36	9.63 ± 0.67
Epoch 2 (+363 days)		
Ion	[Ar II]	[Ar III]
Shell Component		
A_{shell}	0.20 ± 0.01	0.13 ± 0.01
v_{FWHM}	21.51 ± 0.14	19.06 ± 0.33
v_{off}	−2.37 ± 0.03	−2.03 ± 0.08
v_{in}	8.32 ± 0.06	7.68 ± 0.15
v_c	−0.002 ± 0.054	0.22 ± 0.04
Gaussian Components		
A_{blue}	0.009 ± 0.002	0.006 ± 0.002
A_{red}/A_{blue}	0.46 ± 0.17	0.79 ± 0.29
v_{FWHM}	3.50[a]	3.33 ± 0.65
Δv	10.28 ± 0.33	9.86 ± 0.74

Notes. Here, Δv is the separation between peaks; A_{red}/A_{blue} is the red-to-blue Gaussian amplitude ratio. The shell-component parameters are introduced in Table 4, but are refit here with the simple torus model. Velocities and widths are in units of 10^3 km s^{-1}, while amplitudes are given in units of mJy.
[a] Values held to upper limits.

smaller density variations. Due to the degeneracies between the model parameters, the data could support other solutions with the ratio between shell and Gaussian contribution varying more significantly, but we find the constrained solution more physically plausible. The parameters of the constrained fit are given in Table 5. As with previous fits, uncertainties were determined via bootstrap.

This model shows that the line profile corresponds well to a bulk shell-like structure, with overdensities along the line of sight, that combine to a torus-like structure. Measurements of the shell thickness and the separation and widths of the added Gaussian components indicate that the toroidal component extends over the *inner* ∼25% of the shell and lies near the line of sight on opposite sides of the ejecta relative to the observer. Further modeling may determine how inclination and different ejecta density profiles affect this toroidal line profile. We discuss possible implications of these line profiles in Section 5.

5. Discussion and Conclusions

We have presented early- to late-time (−13 days to 1 yr) photometric and spectroscopic observations of SN 2023qov, a nearby, normal SN Ia. Its early-time color and Si II velocity evolution are similar to those of SN 1994D, another fast-declining normal SN Ia. Using our well-sampled photometry, we measure a distance of 36.0 ± 1.8 Mpc, using BayeSN. We present ground-based optical spectra of SN 2023qov spanning 1 yr. Additionally, two epochs (+276 and +363 days) of JWST NIR+MIR spectra are analyzed, with which we make the first robust detection of a dust continuum in a normal SN Ia. We further fit the nebular line profiles of SN 2023qov, and find that it is consistent with other JWST-observed SNe Ia in showing stratified asymmetric shells of IMEs surrounding Gaussian-like IGEs.

The cooling continuum emission detected in the JWST observations of SN 2023qov seems to indicate an IR echo of circumstellar dust heated by radiation from the SN. We do not find clear evidence for dust being freshly formed after the explosion. The direct detection of dust in the MIR spectrum of SN 2023qov is the first such discovery in a normal SN Ia, but previous direct detections of dust in subtypes of SNe Ia have been seen in the SN Ia-CSM 2018evt (L. Wang et al. 2024) and the 03fg-like SN 2022pul (L. A. Kwok et al. 2024; M. R. Siebert et al. 2024). After this discovery in SN 2023qov, reinspection of the JWST spectrum of the normal Type Ia SN 2021aefx presented by L. A. Kwok et al. (2023) reveals potential evidence for a weak dust continuum (see their Figure 1). The existence of dust in SN 2023qov, SN Ia-CSM 2018evt, SN 2022pul, and perhaps SN 2021aefx conflicts with long-held SN Ia theory of a nearly pristine CSM (C. L. Gerardy et al. 2007; H. L. Gomez et al. 2007, 2012). In the case where dust is preexisting, local SN Ia environments are not as pristine as previously thought, and in the case where the dust is formed in the SN explosion, SNe Ia may contribute to the production of interstellar dust along with core-collapse SNe and preexplosion stellar sources, though there is currently little evidence to support the postexplosion scenario.

Fitting the MIR dust continua at the two JWST epochs with various dust models (Section 4.1) confirms that the dust is best fit by blackbody-like carbonaceous dust models, and we measure dust masses on the order of $M_{\rm dust} \approx 10^{-4}\,M_{\odot}$. In the ∼80 days between the two epochs, the dust mass does not change substantially. We do not detect tracers of dust creation, such as carbon monoxide or other molecules often seen in core-collapse SNe (e.g., J. Spyromilio & B. Leibundgut 1996; J. Spyromilio et al. 2001; J. Rho et al. 2009; S. H. Park et al. 2025), or an identifiable second warm dust component (e.g., O. D. Fox et al. 2010). We also cannot identify a significant rebrightening in the late-time optical light curves, as has been seen in some SNe Ia-CSM (e.g., M. L. Graham et al. 2017; K. Tsalapatas et al. 2025). Thus, the dynamical interaction with the ejecta has either not yet occurred, was missed in phases without optical photometry, or is weak.

Our estimated IR light-echo distance (Figure 9) suggests that the dust is within 1 lt-yr of the SN. This alone does not prove that the dust is from the progenitor system, but considering the remote location and elliptical host, little "environmental" dust is expected. Higher-cadence MIR follow-up observations of "dusty" SNe Ia such as SN 2023qov would allow the shell radii, geometry, and composition to be further constrained, with implications for the origin of dust in and around SNe Ia. We summarize the possible physical implications of the dust under each origin scenario below.

1. *Formed by the progenitor.* If the dust is preexisting and involved with the progenitor system, future models must account for the presence of preexisting carbonaceous circumstellar dust. Material may be left over from preexplosion classical nova outbursts (as is seen in cataclysmic variable stars; A. Evans 1990), or winds and unstable mass transfer with some evolved donor star (K. Nomoto & S.-C. Leung 2018). These cases are naturally associated with SD or core-degenerate progenitor scenarios, while comparable mechanisms for producing circumstellar dust in DD systems are less well established (R. Pakmor et al. 2022). The presence of preexisting dust constrains the nature of the progenitor, namely that whatever system preceded SN 2023qov underwent mass loss or outbursts.
2. *Formed by the SN.* Despite the lack of emission from common dust tracers like molecular CO in our observations, the formation of interstellar dust in the ejecta cannot be completely ruled out. Other work (e.g., A. Kumar & A. Sarangi 2026) has already shown that low-luminosity thermonuclear SNe are likely capable of hosting dust formation within hundreds of days. Upon inspection of the late-time optical spectra of the SN (Figure 4), it is not clear whether extinction on the red side of the emission features is present, as would be expected if the dust were formed in the explosion. If the dust detected in SN 2023qov was formed during the explosion, it is worth considering that at least some normal SNe Ia contribute to interstellar dust populations. MIR sampling is required at earlier epochs of other "dusty" SNe Ia, to detect or rule out formation tracers such as CO.
3. *Environmental dust sheet.* Previous SN Ia light echoes that likely occurred in purely environmental dust sheets are SN 1991T (B. P. Schmidt et al. 1994; W. B. Sparks et al. 1999), SN 1998bu (E. Cappellaro et al. 2001), SN 2006X (A. P. S. Crotts & D. Yourdon 2008; X. Wang et al. 2008), and SN 2014J (R. J. Foley et al. 2014; A. P. S. Crotts 2015; Y. Yang et al. 2018). These events occurred in comparatively dusty, star-forming environments. SN 2023qov is in a remote environment

(Figure 1), in which we do not see Na I absorption indicative of a dust-rich local environment, and only exhibits slight reddening (Figure 6). These environmental differences, together with the modeling presented in Section 4.2, favor a circumstellar origin for the dust. If the dust were as far away as an interstellar dust sheet from the SN, it is less likely the SN could have heated it to our measured temperatures. However, owing to the lack of strong constraints on the evolution and geometry of the light echo, we cannot entirely rule out the case of an interstellar dust sheet. If this echo arose from environmental dust, it would suggest that even remote SNe Ia may require nonnegligible host-extinction corrections.

The strong detection of dust in SN 2023qov (as compared with other normal SNe Ia) leads to the consideration that dust may have some effect on SN light curves, in particular the color variation, and thus the standardization of normal SNe Ia. Dust is expected to redden and extinguish optical light, and SN 2023qov has a slightly red light curve a few days postexplosion; however, the extent to which the early light curve is reddened by possibly preexisting dust is unclear. M. Bulla et al. (2018) determined that the reddening is quite sensitive to the dust parameters, which we can now infer via MIR spectra. Using this to analyze the reddening of a wider population will allow for robust characterization of the color variation caused by dust. This will expand physical interpretations for the empirical color corrections made for cosmological analyses. It may further clarify the existing degeneracies between line-of-sight host extinction, preexisting circumstellar dust emission and extinction, and the intrinsic color of the SN. A concrete determination of the cosmological implications of dust in SNe Ia will require the continued expansion of the sample of normal SN Ia observed by JWST in the MIR.

In addition to the dust emission, SN 2023qov shows strong stable nickel emission in the NIR and MIR nebular phases. The light curves of normal SNe Ia are primarily powered by the radioactive decay of ^{56}Ni into ^{56}Co and at later times from ^{56}Co into ^{56}Fe. At nebular times, all ^{56}Ni will have already decayed, so nebular Ni lines trace stable Ni (^{58}Ni, ^{60}Ni, etc.). The stable Ni lines (of which ^{58}Ni is the most abundant isotope) in SN 2023qov have a Gaussian profile, consistent with a central distribution of stable Ni. When compared with other objects in the JWST sample of SNe Ia, SN 2023qov appears to lack the multicomponent broad base plus narrow top Ni II features that are strong in SN 2022aaiq and SN 2024gy (L. A. Kwok et al. 2026). They more closely align with the Gaussian Ni profiles of the 91bg-like (A. V. Filippenko et al. 1992a; B. Leibundgut et al. 1993) SN 2022xkq (J. M. DerKacy et al. 2024). Further, the nickel lines are weaker in amplitude and widths relative to Ar when compared with these normal SN Ia counterparts, being somewhere between them and SN 2022xkq. The formation of this quantity and the distribution of ^{58}Ni in SN 2022aaiq and SN 2024gy may require either the amount of high-density burning present in a near-Chandrasekhar-mass white dwarf (S. Blondin et al. 2022, 2018) or higher metallicities and mixing in a sub-Chandrasekhar-mass white dwarf (K. J. Shen et al. 2018; A. Flörs et al. 2020). The narrower, nearly Gaussian Ni line profiles in SN 2023qov show continued variation in Ni distribution between SNe Ia, which may imply differences in explosion mechanisms. Further MIR sampling of the nickel features of SNe Ia in quiescent environments will help to clarify whether they have a distinct explosion mechanism (i.e., a double detonation) compared with those in star-forming environments. For a more in-depth overview of the implications of stable nickel in SNe Ia, see S. Blondin et al. (2022), S. Kumar et al. (2026), and L. A. Kwok et al. (2026).

In the fits to the NIR and MIR emission lines, we see continued preference for a flat-topped model for the Ar and S lines, similar to SN 2021aefx (L. A. Kwok et al. 2023), SN 2024gy, and SN 2022aaiq (L. A. Kwok et al. 2026). While the fit of a shell model, ideal for the Ar and S lines in these objects, provides a better fit for SN 2023qov than a Gaussian, the profile is double-peaked instead of purely flat-topped (Figure 11). This implies that the emission may arise from an asymmetric ring, rather than a spherical shell of emission (or some combination thereof). L. J. Prust et al. (2025) showed that a similar geometry can arise from companion interaction, with a conical cavity "carved out" by the companion as the ejecta expand. It has not yet been shown, though, that this scenario can fully recreate the toroidal geometry and velocity structure in the IMEs, while having the IGEs continue to appear Gaussian. Regardless, the broad flat-tops of the Ar and S lines—in comparison with the narrower Gaussian-shaped Ni and Co lines—indicate stratified ejecta, with IMEs located outside an IGE-dominated core.

The emission-line morphology and the presence of dust in SN 2023qov could hint at the cause of the variances in evolutionary characteristics among normal SNe Ia. Asymmetries in the ejecta can cause viewing-angle-dependent changes to the light curve, as well as the possibility of reddening due to dust. Concrete conclusions linking photometric properties, such as color, decline rate, and brightness, to NIR and MIR spectral characteristics, including these line asymmetries and the presence of circumstellar dust, will require a larger sample of high-quality late-time JWST observations of normal SNe Ia.

Acknowledgments

This work is based in part on observations made with the NASA/ESA/CSA James Webb Space Telescope. The data were obtained from the Mikulski Archive for Space Telescopes at the Space Telescope Science Institute (STScI), which is operated by the Association of Universities for Research in Astronomy (AURA), Inc., under NASA contract NAS5-03127 for JWST. These observations are associated with JWST program GO-4516 (PI: S. W. Jha). The specific observations analyzed can be accessed via doi:10.17909/6h34-tq75.

The SALT data presented here were obtained with Rutgers University programs 2023-1-MLT-008, 2024-1-MLT-003 (PI: S. W. Jha), and 2024-1-MLT-004 (PI: L. Kwok). We thank Rudi Kuhn, Antoine Mahoro, Moses Mogotsi, and Lee Townsend for making these observations. This work makes use of data from the Las Cumbres Observatory network. The LCO team is supported by NSF grant AST-2308113. Based in part on data acquired at the ANU 2.3 m telescope. The automation of the telescope was made possible through an initial grant provided by the Centre of Gravitational Astrophysics and the Research School of Astronomy and Astrophysics at the Australian National University and through a grant provided by the Australian Research Council through LE230100063. We acknowledge the traditional custodians of the land on which the telescope stands, the Gamilaraay people, and pay our respects to elders past and present. We also used

observations collected at the European Southern Observatory under ESO program 114.27JL.001, and the European Organisation for Astronomical Research in the Southern Hemisphere under ESO program 114.27JL. This work was supported by the "Action Thématique de Physique Stellaire" (ATPS) of CNRS/INSU PN Astro cofunded by CEA and CNES. Some of the data presented herein were obtained at the W. M. Keck Observatory, which is operated as a scientific partnership among the California Institute of Technology, the University of California, and NASA; the observatory was made possible by the generous financial support of the W. M. Keck Foundation.

C.W.M. acknowledges support by the National Science Foundation Graduate Research Fellowship Program under grant 2444108. JWST and ground-based supernova research at Rutgers University is supported by awards JWST-GO-02072 and NSF AST-2407567, respectively. S.W.J. is also grateful for support from a Guggenheim Fellowship. C.L. acknowledges funding through JWST program grants GO-06541, GO-06585, and GO-05324. Support for M.D. was provided by Schmidt Sciences, LLC. L.A.K. is supported by NASA through Hubble Fellowship grant HF2-51579.001-A awarded by STScI, which is operated by AURA, Inc., under contract NAS5-26555 for NASA.

Time-domain research by the University of Arizona team and D.J.S. is supported by NSF grants AST-2308181, 2407566, and 2432036. B.B. has received support from the Hungarian National Research, Development and Innovation Office grants OTKA PD-147091 and from the HUN-REN Hungarian Research Network. C.B. acknowledges support from Chandra Theory grants TM0-21004X and TM1-22004X, XRISM Guest Scientist grant 80NSSC23K0634, and NSF grants AST-2307865 and 2511539. S.H. thanks the LSST-DA Data Science Fellowship Program, which is funded by LSST-DA, the Brinson Foundation, the WoodNext Foundation, and the Research Corporation for Science Advancement Foundation; her participation in the program has benefited this work. A.J. acknowledges support by the Swedish Research Council (grant 2018–03799).

K.Mae. was supported by Japan Society for the Promotion of Science (JSPS) KAKENHI grants JP24KK0070 and JP24H01810. K.Mag. acknowledges funding from Horizon Europe ERC grant 101125877. M.R.S. is supported by an STScI Postdoctoral Fellowship. T.T. acknowledges support from NSF grant AST-2205314 and NASA ADAP award 80NSSC23K1130. J.H.T. acknowledges Horizon Europe ERC grant 101125877. M.S. acknowledges financial support provided under the National Post Doctoral Fellowship (N-PDF; File Number PDF/2023/002244) by the Science & Engineering Research Board (SERB), Anusandhan National Research Foundation (ANRF), Government of India. J.V. is supported by Hungarian NKFIH-OTKA grant K142534. L.Z. W. is sponsored by the National Natural Science Foundation of China (NSFC) grant 12573050, the Chinese Academy of Sciences South America Center for Astronomy (CASSACA) Key Research Project E52H540301, and the Chinese Academy of Sciences (CAS) through a grant to the CASSACA. The work of X.W. is supported by NSFC grants 12288102 and 12033003, the Ma Huateng Foundation, and the New Cornerstone Science Foundation through the XPLORER PRIZE.

A.V.F.'s research group at UC Berkeley acknowledges financial assistance from the Christopher R. Redlich Fund, Gary and Cynthia Bengier, Clark and Sharon Winslow, Alan Eustace and Kathy Kwan (W.Z. is a Bengier-Winslow-Eustace Specialist in Astronomy), Timothy and Melissa Draper, Briggs and Kathleen Wood, Ellyn and Alan Seelenfreund (T.G.B. is Draper-Wood-Seelenfreund Specialist in Astronomy), and numerous other donors.

Facilities: ATLAS, JWST (NIRSpec/MIRI), SALT (RSS).

Software: Astropy (Astropy Collaboration et al. 2013, 2018, 2022), BayeSN (K. S. Mandel et al. 2022), Matplotlib (J. D. Hunter 2007), NED Extinction Calculator,[46] Numpy (C. R. Harris et al. 2020), Pandas (The pandas development team 2020), PyRAF (Science Software Branch at STScI 2012), PySALT (S. M. Crawford et al. 2010), jwst (H. Bushouse et al. 2022), Scipy (P. Virtanen et al. 2020), SNCosmo (K. Barbary et al. 2016), `SNooPy` (C. R. Burns et al. 2011). Jupyter notebooks used to complete this work are available upon request.

ORCID iDs

Colin W. Macrie https://orcid.org/0000-0002-9209-2787
Conor Larison https://orcid.org/0000-0003-2037-4619
Huei Sears https://orcid.org/0000-0001-8023-4912
Lindsey A. Kwok https://orcid.org/0000-0003-3108-1328
Saurabh W. Jha https://orcid.org/0000-0001-8738-6011
Mi Dai https://orcid.org/0000-0001-5694-3399
Joel Johansson https://orcid.org/0000-0001-5975-290X
Stéphane Blondin https://orcid.org/0000-0002-9388-2932
Moira Andrews https://orcid.org/0000-0002-1895-6639
K. Auchettl https://orcid.org/0000-0002-4449-9152
Carles Badenes https://orcid.org/0000-0003-3494-343X
Barnabás Barna https://orcid.org/0000-0003-4769-4794
K. Azalee Bostroem https://orcid.org/0000-0002-4924-444X
Thomas G. Brink https://orcid.org/0000-0001-5955-2502
Kyle W. Davis https://orcid.org/0000-0002-5680-4660
Joseph R. Farah https://orcid.org/0000-0003-4914-5625
Alexei V. Filippenko https://orcid.org/0000-0003-3460-0103
Ori D. Fox https://orcid.org/0000-0003-2238-1572
Or Graur https://orcid.org/0000-0002-4391-6137
Saarah Hall https://orcid.org/0000-0002-3841-380X
D. Andrew Howell https://orcid.org/0000-0003-4253-656X
Griffin Hosseinzadeh https://orcid.org/0000-0002-0832-2974
Anders Jerkstrand https://orcid.org/0000-0001-8005-4030
Réka Könyves-Tóth https://orcid.org/0000-0002-8770-6764
C. Lidman https://orcid.org/0000-0003-1731-0497
Keiichi Maeda https://orcid.org/0000-0003-2611-7269
Kate Maguire https://orcid.org/0000-0002-9770-3508
Bailey Martin https://orcid.org/0009-0006-4963-3206
Adam Miller https://orcid.org/0000-0001-9515-478X
Megan Newsome https://orcid.org/0000-0001-9570-0584
Estefania Padilla Gonzalez https://orcid.org/0000-0003-0209-9246
Abigail Polin https://orcid.org/0000-0002-1633-6495
Armin Rest https://orcid.org/0000-0002-4410-5387
Zoe A. Rosenberg https://orcid.org/0009-0006-0764-8856

[46] github.com/mmechtley/ned_extinction_calc

David J. Sand https://orcid.org/0000-0003-4102-380X
Michaela Schwab https://orcid.org/0009-0002-5096-1689
Matthew R. Siebert https://orcid.org/0000-0003-2445-3891
Mridweeka Singh https://orcid.org/0000-0001-6706-2749
Tamás Szalai https://orcid.org/0000-0003-4610-1117
Tea Temim https://orcid.org/0000-0001-7380-3144
Jacco H. Terwel https://orcid.org/0000-0001-9834-3439
Brad E. Tucker https://orcid.org/0000-0002-4283-5159
József Vinkó https://orcid.org/0000-0001-8764-7832
Lingzhi Wang https://orcid.org/0000-0002-1094-3817
Xiaofeng Wang https://orcid.org/0000-0002-7334-2357
WeiKang Zheng https://orcid.org/0000-0002-2636-6508

References

Aamer, A., Smith, K. W., Srivastav, S., et al. 2023, TNSAN, 236, 1
Arnett, W. D. 1982, ApJ, 253, 785
Ashall, C., Hoeflich, P., Baron, E., et al. 2024, ApJ, 975, 203
Ashall, C., Lu, J., Shappee, B. J., et al. 2022, ApJL, 932, L2
Astropy Collaboration, Price-Whelan, A. M., Lim, P. L., et al. 2022, ApJ, 935, 167
Astropy Collaboration, Price-Whelan, A. M., Sipőcz, B. M., et al. 2018, AJ, 156, 123
Astropy Collaboration, Robitaille, T. P., Tollerud, E. J., et al. 2013, A&A, 558, A33
Barbary, K., Barclay, T., Biswas, R., et al. 2016, SNCosmo: Python library for supernova cosmology, Astrophysics Source Code Library, ascl:1611.017
Bellm, E. C., Kulkarni, S. R., Graham, M. J., et al. 2019, PASP, 131, 018002
Birkmann, S. M., Giardino, G., Sirianni, M., et al. 2022, SPIE, 12180, 121802P
Blasius, T. D., Monnier, J. D., Tuthill, P. G., Danchi, W. C., & Anderson, M. 2012, MNRAS, 426, 2652
Blondin, S. 2026, in Encyclopedia of Astrophysics, ed. I. Mandel (Elsevier), 404
Blondin, S., Bravo, E., Timmes, F. X., Dessart, L., & Hillier, D. J. 2022, A&A, 660, A96
Blondin, S., Dessart, L., & Hillier, D. J. 2018, MNRAS, 474, 3931
Blondin, S., Dessart, L., Hillier, D. J., Ramsbottom, C. A., & Storey, P. J. 2023, A&A, 678, A170
Blondin, S., & Tonry, J. L. 2007, ApJ, 666, 1024
Branch, D., Romanishin, W., & Baron, E. 1996, ApJ, 465, 73
Brown, P. J., Breeveld, A. A., Holland, S., Kuin, P., & Pritchard, T. 2014, Ap&SS, 354, 89
Bulla, M., Goobar, A., Amanullah, R., Feindt, U., & Ferretti, R. 2018, MNRAS, 473, 1918
Burns, C. R., Stritzinger, M., Phillips, M. M., et al. 2011, AJ, 141, 19
Burns, C. R., Stritzinger, M., Phillips, M. M., et al. 2014, ApJ, 789, 32
Bushouse, H., Eisenhamer, J., Dencheva, N., et al. 2022, JWST Calibration Pipeline, v1.8.2, Zenodo, doi:10.5281/zenodo.7325378
Cappellaro, E., Mazzali, P. A., Benetti, S., et al. 1997, A&A, 328, 203
Cappellaro, E., Patat, F., Mazzali, P. A., et al. 2001, ApJL, 549, L215
Chomiuk, L., Soderberg, A. M., Chevalier, R. A., et al. 2016, ApJ, 821, 119
Court, T., Badenes, C., Lee, S.-H., Patnaude, D., & Bravo, E. 2026, ApJ, 996, 100
Crawford, S. M., Still, M., Schellart, P., et al. 2010, SPIE, 7737, 773725
Crotts, A. P. S. 2015, ApJL, 804, L37
Crotts, A. P. S., & Yourdon, D. 2008, ApJ, 689, 1186
DerKacy, J. M., Ashall, C., Hoeflich, P., et al. 2023, ApJL, 945, L2
DerKacy, J. M., Ashall, C., Hoeflich, P., et al. 2024, ApJ, 961, 187
Dhawan, S., Leibundgut, B., Spyromilio, J., & Blondin, S. 2016, A&A, 588, A84
Dopita, M., Hart, J., McGregor, P., et al. 2007, Ap&SS, 310, 255
Dopita, M., Rhee, J., Farage, C., et al. 2010, Ap&SS, 327, 245
Draine, B. T. 2011, Physics of the Interstellar and Intergalactic Medium (Princeton Univ. Press)
Draine, B. T., & Lee, H. M. 1984, ApJ, 285, 89
Draine, B. T., & Li, A. 2007, ApJ, 657, 810
Evans, A. 1990, IAUC, 122, 253
Filippenko, A. V. 1982, PASP, 94, 715
Filippenko, A. V., Richmond, M. W., Branch, D., et al. 1992a, AJ, 104, 1543
Filippenko, A. V., Richmond, M. W., Matheson, T., et al. 1992b, ApJL, 384, L15
Fink, M., Röpke, F. K., Hillebrandt, W., et al. 2010, A&A, 514, A53
Flörs, A., Spyromilio, J., Taubenberger, S., et al. 2020, MNRAS, 491, 2902
Foley, R. J., Challis, P. J., Chornock, R., et al. 2013, ApJ, 767, 57
Foley, R. J., Fox, O. D., McCully, C., et al. 2014, MNRAS, 443, 2887
Foley, R. J., Papenkova, M. S., Swift, B. J., et al. 2003, PASP, 115, 1220
Foreman-Mackey, D., Hogg, D. W., Lang, D., & Goodman, J. 2013, PASP, 125, 306
Fox, O. D., Chevalier, R. A., Dwek, E., et al. 2010, ApJ, 725, 1768
Fox, O. D., & Filippenko, A. V. 2013, ApJL, 772, L6
Fox, O. D., Johansson, J., Kasliwal, M., et al. 2016, ApJL, 816, L13
Fransson, C., & Jerkstrand, A. 2015, ApJL, 814, L2
Freudling, W., Romaniello, M., Bramich, D. M., et al. 2013, A&A, 559, A96
Garnavich, P., Wood, C. M., Milne, P., et al. 2023, ApJ, 953, 35
Gerardy, C. L., Meikle, W. P. S., Kotak, R., et al. 2007, ApJ, 661, 995
Ginolin, M., Rigault, M., Smith, M., et al. 2025, A&A, 695, A140
Gomez, H. L., Clark, C. J. R., Nozawa, T., et al. 2012, MNRAS, 420, 3557
Gomez, H. L., Eales, S. A., & Dunne, L. 2007, IJAsB, 6, 159
Graham, M. L., Harris, C. E., Fox, O. D., et al. 2017, ApJ, 843, 102
Guy, J., Astier, P., Baumont, S., et al. 2007, A&A, 466, 11
Guy, J., Astier, P., Nobili, S., Regnault, N., & Pain, R. 2005, A&A, 443, 781
Hamuy, M., Phillips, M. M., Suntzeff, N. B., et al. 1996, AJ, 112, 2391
Hamuy, M., Trager, S. C., Pinto, P. A., et al. 2000, AJ, 120, 1479
Harris, C. R., Millman, K. J., van der Walt, S. J., et al. 2020, Natur, 585, 357
Hicken, M., Challis, P., Jha, S., et al. 2009, ApJ, 700, 331
Höflich, P. 1995, ApJ, 443, 89
Holoien, T. W.-S., Stanek, K. Z., Kochanek, C. S., et al. 2017, MNRAS, 464, 2672
Hosseinzadeh, G., Sand, D. J., Sarbadhicary, S. K., et al. 2023, ApJL, 953, L15
Howell, D. A., Sullivan, M., Nugent, P. E., et al. 2006, Natur, 443, 308
Hoyle, F., & Fowler, W. A. 1960, ApJ, 132, 565
Hunter, J. D. 2007, CSE, 9, 90
Itagaki, K. 2020, TNSTR, 2020-5, 1
Jäger, C., Mutschke, H., & Henning, T. 1998, A&A, 332, 291
Jakobsen, P., Ferruit, P., Alves de Oliveira, C., et al. 2022, A&A, 661, A80
Jerkstrand, A., Ergon, M., Smartt, S. J., et al. 2015, A&A, 573, A12
Jha, S. W., Badenes, C., Camacho-Neves, Y., et al. 2024, JWST Proposal, Cycle 3, #6580
Jha, S. W., Maguire, K., & Sullivan, M. 2019, NatAs, 3, 706
Johansson, J., Amanullah, R., & Goobar, A. 2013, MNRAS, 431, L43
Kendrew, S., Scheithauer, S., Bouchet, P., et al. 2015, PASP, 127, 623
Kendrew, S., Scheithauer, S., Bouchet, P., et al. 2016, SPIE, 9904, 990443
Kenworthy, W. D., Jones, D. O., Dai, M., et al. 2021, ApJ, 923, 265
Kumar, A., & Sarangi, A. 2026, ApJ, 999, 234
Kumar, S., Hsiao, E. Y., Ashall, C., et al. 2026, ApJ, 1000, 178
Kwok, L. A., Jha, S. W., Temim, T., et al. 2023, ApJL, 944, L3
Kwok, L. A., Liu, C., Jha, S. W., et al. 2026, ApJ, 1005, 52
Kwok, L. A., Siebert, M. R., Johansson, J., et al. 2024, ApJ, 966, 135
Kwok, L. A., Singh, M., Jha, S. W., et al. 2025, ApJL, 989, L33
Larison, C., Jha, S. W., Kwok, L. A., & Camacho-Neves, Y. 2024, ApJ, 961, 185
Leibundgut, B., Kirshner, R. P., Phillips, M. M., et al. 1993, AJ, 105, 301
Li, L., Wang, Z., Liu, J., et al. 2026, ApJ, 996, 10
Lira, P. 1996, MS thesis, Univ. Chile
Liu, Z.-W., Röpke, F. K., & Han, Z. 2023, RAA, 23, 082001
Maeda, K., Nozawa, T., Nagao, T., & Motohara, K. 2015, MNRAS, 452, 3281
Mandel, K. S., Thorp, S., Narayan, G., Friedman, A. S., & Avelino, A. 2022, MNRAS, 510, 3939
Mo, G., De, K., Wiston, E., et al. 2025, ApJL, 980, L33
Morgan, H. L., & Edmunds, M. G. 2003, MNRAS, 343, 427
Morrell, N., Phillips, M. M., Folatelli, G., et al. 2024, ApJ, 967, 20
Newman, M. J. B., Larison, C., Jha, S. W., et al. 2026, ApJ, 1006, 178
Nomoto, K., Kobayashi, C., & Tominaga, N. 2013, ARA&A, 51, 457
Nomoto, K., & Leung, S.-C. 2018, SSRv, 214, 67
Nomoto, K., Thielemann, F. K., & Wheeler, J. C. 1984, ApJL, 279, L23
Ogando, R. L. C., Maia, M. A. G., Pellegrini, P. S., & da Costa, L. N. 2008, AJ, 135, 2424
Oke, J. B., Cohen, J. G., Carr, M., et al. 1995, PASP, 107, 375
Padilla Gonzalez, E., Farah, J., Howell, D. A., et al. 2023, TNSCR, 2023-2054, 1
Padilla Gonzalez, E., Joshi Bhavin, A., Strolger, L. G., et al. 2026, ApJ, 1001, 95
Pakmor, R., Callan, F. P., Collins, C. E., et al. 2022, MNRAS, 517, 5260
Pakmor, R., Kromer, M., Taubenberger, S., et al. 2012, ApJL, 747, L10
Park, S. H., Rho, J., Yoon, S.-C., et al. 2025, A&A, 703, A227
Patat, F., Benetti, S., Cappellaro, E., et al. 1996, MNRAS, 278, 111
Perley, D. A. 2019, PASP, 131, 084503

Perlmutter, S., Aldering, G., Goldhaber, G., et al. 1999, ApJ, 517, 565
Phillips, M. M. 1993, ApJ, 413, L105
Phillips, M. M., Lira, P., Suntzeff, N. B., et al. 1999, AJ, 118, 1766
Prust, L. J., Kumar, G., & Bildsten, L. 2025, ApJ, 982, 60
Rho, J., Reach, W. T., Tappe, A., et al. 2009, ApJ, 700, 579
Riess, A. G., Filippenko, A. V., Challis, P., et al. 1998, AJ, 116, 1009
Riess, A. G., Macri, L. M., Hoffmann, S. L., et al. 2016, ApJ, 826, 56
Rigault, M., Brinnel, V., Aldering, G., et al. 2020, A&A, 644, A176
Rigault, M., Copin, Y., Aldering, G., et al. 2013, A&A, 560, A66
Rigault, M., Smith, M., Regnault, N., et al. 2025, A&A, 694, A2
Rigby, J., Perrin, M., McElwain, M., et al. 2023, PASP, 135, 048001
Rouleau, F., & Martin, P. G. 1991, ApJ, 377, 526
Ruiter, A. J., & Seitenzahl, I. R. 2025, A&ARv, 33, 1
Sand, D. J., Brown, T., Haynes, R., & Dubberley, M. 2011, AAS Meeting, 218, 132.03
Schlafly, E. F., & Finkbeiner, D. P. 2011, ApJ, 737, 103
Schlegel, E. M. 1990, MNRAS, 244, 269
Schmidt, B. P., Kirshner, R. P., Leibundgut, B., et al. 1994, ApJL, 434, L19
Science Software Branch at STScI 2012, PyRAF: Python alternative for IRAF, Astrophysics Source Code Library, ascl:1207.011
Seitenzahl, I. R., Ciaraldi-Schoolmann, F., Röpke, F. K., et al. 2013, MNRAS, 429, 1156
Senzel, R., Maguire, K., Burgaz, U., et al. 2025, A&A, 694, A14
Shen, K. J., Kasen, D., Miles, B. J., & Townsley, D. M. 2018, ApJ, 854, 52
Siebert, M. R., Dimitriadis, G., Polin, A., & Foley, R. J. 2020, ApJL, 900, L27
Siebert, M. R., Kwok, L. A., Johansson, J., et al. 2024, ApJ, 960, 88
Silverman, J. M., Foley, R. J., Filippenko, A. V., et al. 2012, MNRAS, 425, 1789
Silverman, J. M., Vinkó, J., Marion, G. H., et al. 2015, MNRAS, 451, 1973
Smith, M. P., Nordsieck, K. H., Burgh, E. B., et al. 2006, SPIE, 6269, 62692A
Sparks, W. B., Macchetto, F., Panagia, N., et al. 1999, ApJ, 523, 585
Spyromilio, J., & Leibundgut, B. 1996, MNRAS, 283, L89
Spyromilio, J., Leibundgut, B., & Gilmozzi, R. 2001, A&A, 376, 188
Sullivan, M., Conley, A., Howell, D. A., et al. 2010, MNRAS, 406, 782
Sullivan, M., Le Borgne, D., Pritchet, C. J., et al. 2006, ApJ, 648, 868
Tartaglia, L., Sand, D. J., Valenti, S., et al. 2018, ApJ, 853, 62
The pandas development team 2022, pandas-dev/pandas: Pandas, v3.0.5, Zenodo, Zenodo, doi:10.5281/zenodo.3509134
Thielemann, F.-K., Nomoto, K., & Yokoi, K. 1986, A&A, 158, 17
Tinyanont, S., Foley, R. J., Taggart, K., et al. 2024, PASP, 136, 014201
Tonry, J. L., Denneau, L., Heinze, A. N., et al. 2018, PASP, 130, 064505
Tripp, R. 1998, A&A, 331, 815
Tsalapatas, K., Sollerman, J., Chiba, R., et al. 2025, A&A, 704, A135
Valenti, S., Sand, D., Pastorello, A., et al. 2014, MNRAS, 438, L101
Virtanen, P., Gommers, R., Oliphant, T. E., et al. 2020, NaMet, 17, 261
Wang, L., Hu, M., Wang, L., et al. 2024, NatAs, 8, 504
Wang, X., Chen, J., Wang, L., et al. 2019, ApJ, 882, 120
Wang, X., Filippenko, A. V., Ganeshalingam, M., et al. 2009, ApJL, 699, L139
Wang, X., Li, W., Filippenko, A. V., et al. 2008, ApJ, 677, 1060
Wang, X., Wang, L., Filippenko, A. V., Zhang, T., & Zhao, X. 2013, Sci, 340, 170
Wojtak, R., Hjorth, J., & Hjortlund, J. O. 2023, MNRAS, 525, 5187
Yang, Y., Wang, L., Baade, D., et al. 2018, ApJ, 852, 89
Zubko, V. G., Mennella, V., Colangeli, L., & Bussoletti, E. 1996, MNRAS, 282, 1321